Re-submitted to Physics of The Earth and Planetary Interiors
22 June 2010

Rheological contrast between garnet and clinopyroxene in the mantle wedge: an example from Higashi-akaishi peridotite mass, SW Japan

Masashi Muramoto[1], Katsuyoshi Michibayashi[1]*, Jun-ichi Ando[2], Hiroyuki Kagi[3]

[1]*Institute of Geosciences, Shizuoka University, Shizuoka 422-8529, Japan*
[2]*Department of Earth and Planetary Systems Science, Hiroshima University, Hiroshima 739-8526, Japan*
[3]*Laboratory of Earthquake Chemistry, The University of Tokyo, Tokyo 113-0033, Japan*

*Corresponding author: sekmich@ipc.shizuoka.ac.jp

Abstract

Garnet clinopyroxenites occur within foliated dunite in the Higashi-akaishi peridotite mass, located within the subduction-type high-pressure/low-temperature Sanbagawa metamorphic belt. The garnet clinopyroxenites contain 3–80% garnet, and garnet and clinopyroxene are homogeneously distributed. Garnet crystals contain extensive, regular dislocation arrays and dislocation networks, suggesting that dislocation creep was the dominant deformation mechanism. Analyses of crystallographic orientation maps indicate similar grain sizes and aspect ratios for garnet and clinopyroxene, regardless of modal composition, indicating that these minerals deformed with similar degree of plasticity. However, indexes of crystallographic fabric intensity (i.e., *J*-index and *M*-index) for both garnet and clinopyroxene tend to increase with increasing modal composition of garnet~~, suggesting that the two minerals deformed under similar degree of plasticity~~. Fourier-transform infrared spectroscopy analysis revealed that water content in garnet is ~60 ppm, whereas that in clinopyroxene is ~70 ppm, whereas olivine crystal-preferred orientations in the Higashi-akaishi peridotite mass, characterized by [001](010), are thought to have developed during deformation under wet conditions. Consequently, we argue that the presence of water could act to enhance garnet plasticity during deformation. The results reveal contrasting influences of water on the deformation of garnet and diopside: under wet conditions compared with dry, the strain rate increases by two orders of magnitude for garnet but by an order of magnitude for diopside. Given the influence of water on the creep strength of garnet, garnet within the Higashi-akaishi mass may have become significantly as weak as clinopyroxene during deformation.

Key words: garnet, clinopyroxene, olivine, water, rheology, dislocation, EPMA, EBSD, TEM, FTIR, crystal-preferred orientation (CPO), Higashi-akaishi peridotite

1. Introduction

Garnet is a major constituent mineral of the lower continental crust, in subducting oceanic crust, and in the mantle transition zone. Moreover, in the mid-mantle, garnet is a volumetrically important mineral, as pyrolite mantle contains up to 40% garnet, whereas subducted oceanic crust contain up to 90% garnet in the transition zone (410-670 km depth) (Ringwood, 1982). The rheological behavior of garnet is therefore an important factor in the deformation of subducted oceanic crust and lower continental crust.

Because garnet commonly behaves as a rigid object during crustal deformation, it is generally thought to have a higher creep strength than that of minerals such as quartz and feldspar. This view is supported by the results of experimental deformation of garnet; accordingly, the high strength of garnet is explained by high resistance to dislocation glide due to very large Burgers vectors (Karato *et al*., 1995). Nevertheless, several reports have presented the ductile deformation of garnet in naturally deformed rocks (Dalziel and Bailey, 1968; Ando *et al*., 1993; Doukhan *et al*., 1994; Ji and Martignole, 1994). Recent studies have investigated the nature of garnet plasticity using a combination of optical microscopy, scanning electron microscopy (SEM), electron backscattered diffraction (EBSD), and transmission electron microscopy (TEM) (e.g., Kleinschodt and McGrew, 2000; Prior *et al*., 2000; Ji *et al*., 2003; Michibayashi *et al*., 2004; Okamoto and Michibayashi, 2005; Storey and Prior, 2005; Li et al., 2006; Zhang and Green, 2007). Ji *et al*. (2003) showed that the rheological contrast between garnet and omphacite under ultra-high pressure (UHP) conditions is smaller than that commonly observed between garnet and clinopyroxene in typical deep crustal rocks; however, little is known about the rheological behavior of garnet.

Here, we present the results of field studies, optical and TEM observations, and EBSD measurements of garnet clinopyroxenites collected from the Higashi-akaishi peridotite mass in the Sanbagawa metamorphic belt, central Shikoku, Japan. Based on these results, we discuss the rheological behavior of garnet along with olivine and clinopyroxene under high temperatures and pressures.

2. Geological setting

The Sanbagawa belt of Southwest Japan (Fig. 1a) is one of the most well-documented examples of a subduction-type high-pressure/temperature metamorphic body. The belt consists mainly of meta-sedimentary and meta-volcanic rocks that originated in

oceanic environments and were subsequently metamorphosed during Cretaceous subduction. The Sanbagawa belt is bounded to the north by the Ryoke belt, which is characterized by low-pressure/temperature metamorphism. Together, these belts constitute what is perhaps the most well-known example of a paired metamorphic belt (Miyashiro, 1961).

The boundary between the Sanbagawa and Ryoke belts is a major strike-slip fault, the Median Tectonic Line (MTL). The Sanbagawa belt is divided into chlorite, garnet, albite–biotite, and oligoclase–biotite zones (in order of increasing metamorphic grade) based on the mineral paragenesis of pelitic schists (Enami, 1983; Higashino, 1990). The high-grade albite–biotite and oligoclase–biotite zones are widely distributed throughout the Besshi region of central Shikoku (Fig. 1a, b), where they are divided into the Besshi unit and a series of high-pressure (HP) bodies that record eclogite facies metamorphism (Takasu, 1989). The metamorphic history of the Besshi unit is characterized by a series of clockwise pressure–temperature paths involving an increase in temperature subsequent to peak metamorphic pressure (0.6–1.1 GPa; Enami *et al*., 1994; Aoya, 2001). The HP eclogite bodies consist mainly of mafic and ultramafic lithologies. The mafic rocks are schistose or consist of massive garnet-bearing epidote–amphibolites with local relic eclogite. These bodies are distinguished from the Besshi unit by significantly higher peak metamorphic pressures (above 1.5 GPa; e.g., Takasu, 1989; Wallis *et al*., 2000) and the fact that they structurally overlie the Besshi unit (Wallis and Aoya, 2000).

The Higashi-akaishi mass, which is the largest ultramafic lens (5 × 1.5 km) in the Sanbagawa belt (Fig. 1b), contains dunite, wehrlite, and garnet clinopyroxenite. (Horikoshi, 1937; Yoshino, 1961; Mori and Banno, 1973; Enami *et al*., 2004; Mizukami *et al*., 2004; Hattori et al., 2010). Thermobarometric analyses of the garnet-bearing rocks indicate UHP conditions above 3 GPa (Enami *et al*., 2004). Four distinct phases of deformation (D1–D4) are recognized in the mass (Mizukami and Wallis, 2005). The tectonic significance of D1 is unclear, whereas D2 represents the dominant deformation fabric in the Higashi-akaishi mass. Microstructural observations, combined with the results of garnet–orthopyroxene geothermobarometry, suggest that D2 took place during high-temperature subduction down to depths of ~100 km (above 2.8 GPa at temperatures of 700–800 °C) or more. D3 represents a major phase of exhumation, after which the Higashi-akaishi mass was juxtaposed with the adjacent Besshi and Eclogite units at a

depth of around 35 km (1 GPa). D4 corresponds to a stage of intertectonic growth of plagioclase in the Besshi and Eclogite units.

3. Field observations

The dominant rock type within the Higashi-akaishi peridotite mass is dunite, which is classified into massive dunite and foliated dunite based on field observations. Massive dunite occurs around the top of Higashi-Akaishi Mountain (Figs. 1c and 2a), whereas foliated dunite occurs in the Gongen Pass, at the northeast marginal zone of the Higashi-Akaishi peridotite mass (Figs. 1c and 2b). In the Gongen Pass, peridotites are strongly sheared and mylonitized, producing a strong foliation (Fig. 2b, d). Some dunites that contain a prominent lineation show mullion structures (Fig. 2c). Both types of dunite are fractured and serpentinized to varying degrees.

Samples of garnet clinopyroxenites were collected within Gongen Pass (Fig. 2b). The samples contain 20–80% garnet, and occur within foliated dunites as lenses, boudins, or layers of ~2–50 cm in thickness (e.g., Fig. 2d). Some porphyroclasts in the foliated dunite are mantled by asymmetric tails, resembling σ-type porphyroclasts (Passchier and Simpson, 1986). A σ-type porphyroclast within garnet clinopyroxenite associated with shear bands (C') indicates top-to-the-northwest (north-side-down) displacement (Fig. 2d).

4. Microstructures

Microstructures were analyzed in polished thin sections cut perpendicular to the foliation (Z) and parallel to the lineation (X) (i.e., XZ sections). Foliation and lineation within garnet clinopyroxenite are defined by compositional banding and the shape-preferred orientation of elongate pyroxene crystals (Fig. 3b), whereas foliation and lineation in peridotites are defined by the shape-preferred orientation of elongate spinel (Fig. 3a). We measured the sizes of grains in each sample, and the outlines of approximately 200 grains were carefully traced from photomicrographs of each sample. The area (A) of each grain was then measured using Scion Image software. Grain size (D) was calculated as $D = 2(A/3.14)^{0.5}$ (e.g., Michibayashi and Masuda, 1993; Okamoto and Michibayashi, 2005), representing the diameter of a circle with the same area as that of the grain.

4.1. Peridotites

All of the peridotite samples consist of olivine and Cr-spinel, and are variously serpentinized. Massive dunites show two types of textures. One type is coarse-grained texture (Fig. 4a), in which olivine is ~0.5 mm in size (aspect ratio of ~2) and shows intense undulose extinction and the development of sub-grain boundaries. In some samples, the coarse-grained olivine crystals contain numerous micro-inclusions (Fig. 4d). The second type is porphyroclastic texture (Fig. 4b). Porphyroclasts (~0.4 mm) commonly show evidence of intracrystalline deformation (e.g., kink bands and undulose extinction). In addition, neoblasts (~0.1 mm) are commonly observed near subgrain boundaries in the central parts of olivine porphyroclasts (Fig. 4e). In thin sections oriented parallel to the XY plane, coarse-grained and porphyroclastic olivine grains have average aspect ratios of 1.75 and 1.65, respectively; in YZ sections, the values are 1.60 and 1.65, respectively. Olivine grains are characterized by a quasi-plane-strain shape, with K = ~1 in a Flinn diagram (Fig. 5).

Foliated dunites consist entirely of fine-grained texture (Fig. 4c), with relatively straight grain boundaries that meet at triple junctions. Peridotites from Gongen Pass also consist entirely of fine-grained texture. One sample (GM21) contains a finer-grained layer (~20 μm) composed of olivine and clinopyroxene (Fig. 4f). The aspect ratios of finer-grained olivine are generally ~1.6.

4.2. Garnet clinopyroxenites

4.2.1. Optical observations

The garnet clinopyroxenites are essentially bimineralic, being composed of garnet and clinopyroxene with minor ilmenite. The modal abundance of garnet, as measured using a point-counter, varies from 3 to 80%. Garnet and clinopyroxene show a homogeneous distribution in thin sections (Fig. 6a–c), and both contain numerous inclusions.

Clinopyroxene grains (~0.3 mm) are flattened and elongated (Fig. 6), with some showing well-developed pinch-and-swell structure. Clinopyroxene grains show intense undulose extinction and the development of sub-grain boundaries (Fig. 6d), with aspect ratios of ~2.

4.2.2. Orientation maps

Garnet microstructures were investigated by compiling and analyzing EBSD orientation maps. Data were obtained using a JEOL JSM6300 scanning electron

microscope housed at the Centre for Instrumental Analysis, Shizuoka University, Japan. EBSD patterns were collected on rectangular grids with 10 μm spacing between data points. Patterns were acquired and automatically indexed using the program Channel 5 from HKL software. After an indexing solution was found, or if the software abandoned its attempt to find a solution, the beam was moved 10 μm and a new pattern was collected. Maps were constructed by assigning a color to the pixels representing each measurement point, with the color reflecting the lattice orientation of garnet. In the case that the <100>, <110>, and <111> axes of garnet were oriented parallel to the lineation (X), the grain was colored red, green, or blue, respectively. White areas in the maps are points that were not indexed, or minerals other than garnet. Black lines, representing grain boundaries, are drawn between any adjacent points with a misorientation > 10°.

The orientation maps (Fig. 7c, d) show the occurrence of grain boundaries and fractures. The grain size of garnet is similar to that of clinopyroxene (~0.3 mm). Garnet is flattened and elongated in the garnet clinopyroxenites (Fig. 7c, d), and some grain boundaries consist of interfingering sutures (Fig. 7c, d; Stipp *et al*., 2002). Some garnet grains contain low-angle boundaries (misorientation angles of 2–9°), and aspect ratios are generally ~2, regardless of modal composition.

Garnet clinopyroxenites are pervasively cracked by extensional fractures that are generally oriented perpendicular to the stretching lineation (Figs. 6 and 7). Such lineation-normal fractures are common in granulite facies mylonites and UHP metamorphic rocks, and are thought to form during the final stages of exhumation (Ji *et al*., 1997, 2003).

4.2.3. TEM observations

Single crystals of garnet were hand-picked from crushed samples of garnet clinopyroxenite for TEM observations. TEM samples were thinned using the ion-bombardment technique, and analyzed using a JEOL JEM-2010 (Hiroshima University, Japan) transmission electron microscope at an accelerating voltage of 200 kV. TEM observations of garnet focused on geometrical dislocation microstructures, dislocation densities, and the Burgers vectors of dislocations.

The analyzed garnet grains contain extensive, regular dislocation arrays and dislocation networks. The dislocation arrays (Fig. 8a and b) can be interpreted as tilt subgrain boundaries, while the dislocation networks (Fig. 8c and d) indicate the activation of at least two slip systems. These well-organized dislocation microstructures indicate the occurrence of an efficient diffusion-assisted recovery mechanism such as dislocation

climb or cross slip. The density of free dislocations within garnet ranges from 3 to 6 × 10^7 cm^{-2} (Fig. 9). Dislocation junctions, which are the complex intersections (tangles) of several dislocations, were also observed in each sample (Fig. 8f), indicating interaction between dislocations and therefore the operation of multiple slip systems (Voegelé *et al*., 1998; Wang and Ji, 1999; Ji *et al*., 2003). The above observations are in agreement with previous TEM investigations on naturally deformed garnets (Ando *et al*., 1993; Doukhan *et al*., 1994; Ji and Martignole, 1994; Voegele´ *et al*., 1998; Prior *et al*., 2000; Ji *et al*., 2003), all of which reported that garnet can deform plastically given appropriate conditions of temperature, pressure, differential stress, and strain rate. The Burgers vectors of dislocations were identified using the $\mathbf{g} \cdot \mathbf{b} = 0$ and $\mathbf{g} \cdot \mathbf{b} \times \mathbf{u} = 0$ criteria. The majority of dislocations have a Burgers vector **b** = ½<111>.

5. Electron microprobe analysis

We analyzed the chemical compositions of garnet grains within four samples of garnet clinopyroxenites (Fig. 10) using a JEOL electron microprobe (JXA733) housed at the Centre for Instrumental Analysis, Shizuoka University, Japan. Analytical conditions were 15 kV accelerating voltage, 12 nA probe current, and beam diameter of 20 μm, using a count time of 20 s and 10 s background.

Table 3 lists the results of analyses of 10 representative garnet grains. The grains have similar compositions (Fig. 10a). Microprobe analyses of 75 garnet grains from the four samples yielded the following compositional ranges: 47.3–54.8% pyrope, 27.7–30.9% almandine, 16.7–20.2% grossular, and 0.8–1.6% spessartine, with an average composition of $Alm_{29.9\pm1.4}$ $Prp_{50.5\pm2.6}$ $Grs_{18.6\pm1.8}$ $Spe_{1.0\pm0.3}$. Most of the grains show no significant compositional zoning, although the almandine component shows a slight increase around grain boundaries and cracks, whereas the pyrope component shows a slight decrease.

Clinopyroxene grains are near-homogeneous, contain a diopside component (Fig. 10b), and are compositionally similar among samples.

6. Fourier-transform infrared spectroscopy analysis

We measured the water content in garnet grains using Fourier-transform infrared (FTIR) spectroscopy. For each sample, a polished thin section (~0.25 mm thick) was prepared and dried in an oven at 120 °C for 4 h. The infrared spectrum was obtained using

a Perkin Elmer, Spectrum 2000 (Geochemical Laboratory, University of Tokyo) at room temperature and in the wavenumber range of 740–7800 cm^{-1}. A series of 100 scans was averaged for each spectrum with a resolution of 1 cm^{-1}. For analysis, we carefully selected crack-free and unaltered regions of 60 × 60 μm^2 in size.

We used FTIR to analyze 38 grains (29 of garnet, 9 of cpx) from four samples. In the typical OH vibration region (3400–3800 cm^{-1}), all grains show several absorption bands. Figure 11 shows typical FTIR spectra of garnet and clinopyroxene from the Higashi-akaishi garnet clinopyroxenite. The infrared (IR) spectra of all garnet grains show a sharp peak at ~3570 cm^{-1} (Fig. 11a); one sample (GM01) shows a peak at ~3430 cm^{-1}, which is typical of the stretching vibrations (ν3+ν1) of molecular water, which may occur in submicroscopic fluid inclusions within garnet. Following previous studies of natural garnets (Rossman and Smyth, 1990; Bell and Rossman, 1992), we ascribed this group of bands to submicroscopic fluid inclusions. The 3570 cm^{-1} peak is produced by structural OH in the garnets. The IR spectra of clinopyroxene show sharp peaks at 3460, 3540, and 3640 cm^{-1} (Fig. 11b), produced by structural OH (Bell *et al*., 1995).

We calculated the water content (H_2O ppm wt.) of both minerals using the Beer–Lambert law (absorbance = absorbance coefficient × thickness × water concentration). Absorbance is expressed as the integrated absorbance areas of OH. We used the following integrated molar absorbance coefficients from Bell *et al*. (1995): 1.39 ppm H_2O/cm^2 for garnet, 7.09 ppm H_2O/cm^2 for clinopyroxene. Table 4 provides detailed information on peak positions, absorbance, and the calculated water content. H_2O contents in garnet range from 17 to 1000 ppm (mainly ~60 ppm) (Fig. 12a). The H_2O content of Higashi-akaishi garnet varies both among and within samples. In contrast, H_2O contents in clinopyroxene are relatively homogeneous within and among samples (~70 ppm)(Fig. 12b).

7. Crystallographic preferred orientations

We measured the crystal-preferred orientations (CPOs) of olivine, garnet, and clinopyroxene grains from highly polished thin sections, using a scanning electron microscope equipped with an electron-backscatter diffraction system (JEOL JSM6300 with HKL Channel5), housed at the Centre for Instrumental Analysis, Shizuoka University, Japan. We measured about 200 crystal orientations per sample, visually confirming the computerized indexation of the diffraction pattern for each orientation. The measured CPOs are presented on equal-area, lower-hemisphere projections in the

structural (XZ) reference frame (Figs. 13–17). To characterize the CPOs, we determined the fabric strength and distribution density of the principal crystallographic axes (e.g., Michibayashi and Mainprice, 2004). The rotation matrix between crystal and sample co-ordinates is used to describe the orientation **g** of a grain or crystal in sample co-ordinates. In practice, it is convenient to describe the rotation by a triplet of Euler angles; e.g., **g** = (φ_1, ϕ, φ_2), as used by Bunge (1982). The orientation distribution function (ODF), f(**g**), is defined as the volume fraction of orientations in the interval between **g** and **g** + d**g** in a space containing all possible orientations, as given by

$$\Delta V / V = \int f(g) dg$$

where $\Delta V/V$ is the volume fraction of crystals with orientation **g**, f(**g**) is the texture function, and $dg = 1/8\pi^2 \sin\phi d\varphi_1 d\phi d\varphi_2$ is the volume of the region of integration in orientation space. To quantify the intensity of a CPO, Mainprice and Silver (1993) proposed the *J*-index, which is defined as follows:

$$J = \int f(g)^2 dg.$$

The *J*-index has a value of unity for a random distribution and a value of infinity for a single crystal. The *J*-index for olivine in our calculations has a maximum of ~250 because of the truncation of the spherical harmonic series at an expansion of 22.

In a similar manner, the intensity of each pole figure can be analytically defined by the *pfJ* index:

$$pfJ = \int P_{hkl}(\alpha, \beta)^2 d\omega$$

where α and β are the spherical co-ordinates of the considered direction in the pole figure, $P_{hkl}(\alpha, \beta)$ is the density in the considered direction for a given crystallographic pole defined by hkl, and $d\omega = 1/2\pi \sin\alpha d\alpha d\beta$ is the volume of the region of integration.

The misorientation index (*M*-index) is defined as the difference between the observed distribution of uncorrelated misorientation angles and the distribution of uncorrelated misorientation angles for a random fabric (Skemer *et al*., 2005):

$$M \equiv \frac{1}{2} \int \left| R^T(\theta) - R^0(\theta) \right| d\theta$$

The calculation is performed for individual bins:

$$M \equiv \sum_{i=1}^{n} \left| R_i^T - R_i^0 \right| \cdot \frac{\theta_{\max}}{2n}$$

where R_i^T is the theoretical distribution of misorientation angles for a random fabric, R_i^0 is the observed distribution of misorientation angles (normalized by the number of data), $\theta_{\max}$ is the maximum theoretical misorientation angle, and n is the number of bins. The factor of 1/2 is used for convenience to ensure that the magnitude of the index increases with fabric strength across the range from 0 (random fabric) to 1 (single crystal fabric). The theoretical distribution for a random fabric depends on crystal symmetry and bin width.

7.1. Olivine CPO

All of the analyzed samples of peridotite show a distinct alignment of [001] axes parallel to the lineation (X), [010] axes normal to the foliation (Z), and [100] axes normal to the lineation and within the plane of the foliation (Y); i.e., a [001](010) CPO pattern (Figs. 13–15). The fabric strength varies from M = 0.029 to 0.340 (J = 2.74 to 10.20).

Two samples with coarse-grained textures show intense [001](010) patterns, characterized by a strong alignment of [010] normal to the foliation (Z) and a strong alignment of [001] close to the lineation (Fig. 13a, d). Three samples with coarse-grained textures show an intense concentration of [010] axes normal to the foliation (Z), with girdles of [100] and [001] axes within the plane of the foliation (XY plane). A weak concentration of [001] axes is seen in the direction parallel to the lineation (X) (Fig. 13b, c, e).

Porphyroclastic textures show relatively weak [001](010) patterns (Fig. 14). For sample HA02, we separately analyzed the CPOs of porphyroclasts and neoblasts. The two sets of grains show similar CPO patterns, although with different fabric intensities (a and c in Fig. 14): porphyroclasts, M = 0.293 (J = 9.29); neoblasts, M = 0.180 (J = 5.60).

Fine-grained textures show very weak [001](010) patterns (Fig. 15), especially GM19 and GM21, which show near-random patterns (Fig. 15e, f).

The fabric intensities determined for all samples are listed in Supplementary Table 1. The trends of the pole figure index *pfJ* generally follow the trends of the *J*-index, with [010] *pfJ* being typically the strongest among the three axes, [001] *pfJ* being intermediate, and [100] *pfJ* being the weakest (Figs. 13–15).

7.2. Garnet CPO

EBSD measurements of more than 200 garnet grains from each sample show weak fabric strengths and complex CPO patterns with numerous maxima of <100>, <111>, and <110> (Fig. 16). The CPO pattern obtained for GM01 is well defined and different from those obtained for the other samples (Fig. 16c). In this sample, <100> poles form three maxima close to the X, Y, and Z directions. The maxima of <110> poles are located diagonally between XY, YZ, and XZ, and the <111> poles diagonally between X, Y, and Z. This pattern corresponds exactly to the end pattern expected for a dominant <100>(010) slip system, which has been reported to be the most likely system in garnet along with 1/2<111>(110), based on TEM analyses of experimentally and naturally deformed garnets (Karato *et al*., 1995; Voegele *et al*., 1998).

The fabric strength data for the analyzed garnets are shown in Table 2 and Fig. 16. The fabric strength varies from M = 0.022 to 0.044 (J = 1.33 to 2.38). Figure 18a shows that fabric strength (M-index) becomes more intense with increasing modal composition of garnet.

7.3. Clinopyroxene CPO

Clinopyroxene shows CPO patterns dominantly characterized by a strong concentration of [001]-axis subparallel to the stretching lineation (X) (Fig 17). (110)-poles, (010)-poles and [100]-axes show a weak concentration normal to the foliations, but their densities varies among the samples (Fig. 17). In sample GM01, girdles of [001] axes slightly oblique to the foliation occur, whereas [010] axes define a complex pattern.

The fabric strength for the clinopyroxene CPO varies from M = 0.048 to 0.087 (J = 4.51 to 7.87) (Table 2). The fabric strength of clinopyroxene shows an increase in intensity with increasing modal composition of garnet (Fig. 18a).

8. Discussion

8.1. Deformation mechanisms recorded by the Higashi-akaishi peridotite mass

Field observations indicate that peridotite within the Higashi-akaishi mass can be classified into massive dunite and foliated dunite. The outcrop within Gongen Pass, which consists of foliated dunite, is strongly deformed. Microstructural observations suggest that peridotites of the Higashi-akaishi mass variably contain coarse-grained texture, porphyroclastic texture, and fine-grained texture. Olivine grains in samples with coarse-grained texture are about 0.5 mm in size, and show intense undulose extinction and the development of sub-grain boundaries. Peridotite deformed by mantle flow typically shows

protogranular texture (Mercier and Nicolas, 1975) with a relatively coarse grain size (3–4 mm). Therefore, the coarse-grained textures (~0.5 mm) of the Higashi-akaishi peridotite could represent a second deformation–recrystallization cycle in the mantle.

Figure 19 shows the average grain size of olivine for each type of texture recognized in the Higashi-akaishi mass. For porphyroclastic texture, we separately measured the grain sizes of porphyroclasts and neoblasts. The grain sizes of coarse- and fine-grained textures are similar to those of porphyroclasts and neoblasts, respectively, and olivine porphyroclasts contain deformation structures (i.e., undulose extinction and sub-grain boundaries). These observations suggest that dynamic recrystallization of pre-existing coarse-grained olivine occurred during the deformation of rocks with porphyroclastic texture. In addition, neoblasts within rocks with porphyroclastic texture are similar in size to fine-grained olivine, suggesting that rocks with fine-grained texture consist entirely of neoblasts. In this case, fine-grained olivine must have been deformed by very high strains. The outcrop within Gongen Pass would be a shear zone developed within rocks of the mantle wedge at depth, as all the peridotites in this outcrop show fine-grained texture.

In general, grain size is expected to change until recrystallized grains attain a steady-state size, which is determined by the magnitude of the deviatoric stress (e.g., Michibayashi et al., 2006). If we assume that the stable mean grain size in the shear zone within Gongen Pass is a steady-state grain size, we can then use grain size as a paleopiezometer with which to infer the magnitude of flow stress (e.g., Van der Wal *et al*., 1993; Jung and Karato, 2001b). The relationship between grain size and differential stress (after Jung and Karato, 2001b) indicates flow stresses for the fine-grained texture of 100 MPa for wet olivine or 40 MPa for dry olivine (Fig. 20).

Mizukami and Wallis (2005) reported four stages of deformation in the Higashi-akaishi peridotite mass (D1–D4). D1 is characterized by the shape-preferred orientation of coarse-grained olivine (~0.6 mm), and is recognized locally in lenticular domains (Fig. 1c). D2, which represents the dominant deformation fabric in the Higashi-akaishi mass, typically displays a porphyroclastic texture consisting of dusty (i.e., inclusion-rich) olivine porphyroclasts (~0.5 mm) and clear (i.e., inclusion-poor) olivine neoblasts (~0.1 mm). The results of garnet–orthopyroxene geothermobarometry indicate P-T conditions of P > 2.1 GPa and T = 750–800 °C for D1 and P > 2.8 GPa and T = 750–800 °C for D2 (Mizukami and Wallis, 2005). This finding suggests that the peridotites with coarse-grained texture and porphyroclastic texture analyzed in the present study correspond to D1 and D2,

respectively. In addition, peridotite with fine-grained textures, as reported in the present study, corresponds to a D2 shear zone.

The olivine CPO patterns measured in the present study indicate that [001](010) slip occurred dominantly throughout the Higashi-akaishi peridotite mass, within rocks with coarse-grained, porphyroclastic, and fine-grained textures (compare Fig. 4 with Figs. 13–15). However, fabric strength varies from M = 0.029 to 0.340 throughout the mass. Figure 21 shows that fabric strength decreases with decreasing olivine grain size, and recrystallized grains show a clear misorientation relative to parent grains (Tommasi *et al*., 2000). Dynamic recrystallization via nucleation and the growth of strain-free neoblasts at grain boundaries may also result in an effective weakening of the CPO (Nicolas and Boudier, 1973; Michibayashi *et al*., 2006). Therefore, we consider that the primary CPO in samples with coarse-grained texture was weakened as a consequence of intense dynamic recrystallization. In previous studies, similar features were reported across shear zones (Michibayashi and Mainprice, 2004; Michibayashi *et al*., 2006; Michibayashi *et al*., 2009). The above findings support the interpretation of the outcrop within Gongen Pass as a D2 shear zone.

Three samples with coarse-grained textures show an intense concentration of [010] axes normal to the foliation (Z), with girdles of [100] and [001] axes within the plane of the foliation (Fig. 13b, c, e). These CPO patterns are compatible with a CPO pattern for D1 sample reported by Mizukami *et al.* (2004). This olivine CPO can be explained based on the results of viscoplastic self-consistent (VPSC) numerical simulations performed by Tommasi *et al*. (1999). The observed pattern is similar to that produced in an axial shortening model; however, the olivine grains in rock with coarse-grained texture are characterized by a quasi-plane-strain shape (Fig. 6), suggesting that the coarse-grained texture resulted from shear strain. Recently, Holtzman *et al*. (2003) reported that such a pattern results from the deformation of melt-depleted lenses; however, the peridotites analyzed in the present study show no evidence of melt. The observed girdles of [100] and [001] axes in Fig. 13 indicate that two slip systems were active, but additional analyses are required to confirm this hypothesis (e.g., TEM observations). The olivine CPO patterns indicate a dominant slip system involving [001](010) slip (Figs. 13-15). This pattern is similar to the B-type pattern described previously (e.g., Jung and Karato, 2001a; Tasaka *et al*., 2008), which is considered to reflect relatively high strain and wet conditions (Jung

and Karato, 2001a; 2006). Accordingly, the Higashi-akaishi peridotite mass may have been deformed under wet conditions (Mizukami et al., 2004).

It is noted that the change in olivine CPO patterns from those observed in the coarse-grained texture (Fig. 13) during the D1 episode at moderate pressure (> 2.1 GPa) to those observed in the porphyroclastic texture (Fig. 14) during the D2 episode at higher pressure (> 2.8 GPa) might be alternatively explained by the effect of increasing pressure on olivine slip system. A pressure-induced olivine slip transition, from dominant [100](010) slip system at low pressure to dominant [001](010) slip system at high pressure, has recently been reported by several authors (e.g., Couvy et al., 2004; Mainprice et al. 2005, Durinck et al., 2005; Jung et al., 2009; Raterron et al., 2007). The olivine slip transition reported by Jung et al. (2009) occurred above 3 GPa, which is nearly compatible with the pressure condition of the D2 episode in the Higashi-Akaishi mass (Mizukami and Wallis, 2005).

8.2. Deformation mechanism in clinopyroxenite

Garnet clinopyroxenites occur in the center of the shear zone within Gongen Pass. Field observations reveal that sheared bodies of garnet clinopyroxenites in foliated dunite are mantled by asymmetric tails to form σ-type structures, and microstructural observations suggest that clinopyroxene grains show intense undulose extinction and the development of sub-grain boundaries. The measured clinopyroxene CPO patterns in Fig. 17 are compatible to the L-type patterns, characterized by (010)-poles in a girdle perpendicular to the lineation and [001]-axes forming a single maximum strongly concentrated in the lineation (Helmstaedt et al., 1972). Bascou et al. (2002) produced L-type patterns in numerical simulations of simple shear. Comparing the clinopyroxene CPO patterns in Fig. 17 with those of Bascou et al. (2002), we found that our data are similar to a relaxed CRSS 1 model in fig. 4 of Bascou et al. (2002), characterized by the dominant [001](100) slip with secondary <110>{010} and [100](010) slips. Therefore, we propose that dislocation creep was the dominant deformation mechanism in clinopyroxene within the Higashi-akaishi garnet clinopyroxenites.

8.3. Deformation mechanisms in garnet

The deformation mechanisms of natural garnet have been debated for many years. A number of studies have reported plastically deformed garnet from granulite, eclogite, and

garnet peridotite rocks (Ando *et al*., 1993; Ji and Martignole, 1994; Kleinschrodt and McGrew, 2000; Ji *et al*., 2003; Michibayashi *et al*., 2004; Terry and Heidelbach, 2004; Okamoto and Michibayashi, 2005; Storey and Prior, 2005; Bestmann *et al*., 2008). Some of these studies have suggested that dislocation creep is the dominant deformation mechanism for garnet, based on TEM observations of dislocation networks and subgrain walls (e.g., Ando *et al*., 1993; Ji and Martignole, 1994; Ji *et al*., 2003); however, the problem exists that although numerical simulations (performed using the VPSC model) of CPO development in garnet produce characteristic CPOs for both axial compression and simple shear deformation (Mainprice *et al*., 2004), very weak or random CPOs patterns are obtained for naturally occurring elongate garnet (Ji *et al*., 2003; Storey and Prior, 2005). Consequently, alternative deformation mechanisms have been proposed. Storey and Prior (2005) suggested that plastic deformation of garnet is dominated by grain-boundary sliding accompanied by subgrain formation and rotation, rather than dislocation creep. Similarly, in an analysis of experimentally deformed eclogites, Zhang and Green (2007) reported the repeated 'sliding off' into the foliation of superficial layers of recrystallized garnet. However, we consider it unlikely that garnet within the Higashi-akaishi mass was deformed in this way, as it shows contrasting textures to those reported in the above studies. For example, Storey and Prior (2005) reported fine recrystallized garnet (~50 μm) around coarse garnet (~1 mm), whereas garnet clinopyroxenites of the Higashi-akaishi mass contain elongate garnet crystals of homogeneous grain size (0.3 mm) (Fig. 7). In addition, some of the grain boundaries observed in the present study consist of interfingering sutures, and the grain size is much coarser than that generally associated with grain-boundary sliding. Therefore, it is difficult to explain the observed garnet deformation in terms of grain-boundary sliding.

Some of the analyzed garnet grains contain low-angle internal boundaries. TEM observations indicate that the garnet grains contain extensive, regular dislocation arrays and dislocation networks, suggesting that the low-angle boundaries are sub-grain boundaries. The density of free dislocations within the analysed garnet grains ranges from 3 to 6×10^7 cm^{-2} (Fig. 9), which is relatively high (Ando *et al*., 1993); however, garnet has low strength and shows complex CPO patterns. Garnet also has a high degree of symmetry and 12 potential slip systems (Ji *et al*., 2003); consequently, any given slip plane needs only undergo a small amount of rotation before the resolved shear stress reaches high levels on a different slip system, such as 1/2 <111> {110}. Although slip

occurs predominantly on {110} planes, it is important to realize that three {110}-type planes intersect in a [111] direction and that screw dislocations with a 1/2 <111> Burgers vector may migrate randomly on {111} planes with high resolved shear stress. Thus, the weakness of garnet CPOs does not provide unequivocal evidence for diffusion creep or against dislocation creep as a deformation mechanism within garnet (Ji *et al*., 2003). Therefore, we propose that dislocation creep was the dominant deformation mechanism in garnet within the Higashi-akaishi garnet clinopyroxenites.

8.4. Rheological contrast between garnet and clinopyroxene

The studied garnet clinopyroxenites are typically bimineralic, being composed of garnet and diopside. Figure 18b shows grain size and aspect ratio data for garnet and diopside within these rocks, with respect to modal composition. Grain sizes and aspect ratios in garnet are comparable with those in clinopyroxene, regardless of the modal composition. Since the garnet clinopyroxenites were plastically sheared along with the foliated dunites, these observations reveal that the two minerals deformed under similar degree of plasticity.

The fabric strength (*M*-index and *J*-index) of a deformed rock is related to finite strain, as the *M*-index (*J*-index) increases with finite plastic strain (Tommasi *et al*., 2000; Skemer *et al*., 2005). Figure 18a shows that the *M*-index of both garnet and clinopyroxene increases with increasing modal composition of garnet. Because the distribution of garnet and clinopyroxene is homogeneous in the analyzed samples (Fig. 6), the dominant phase controls the deformation of the rock. If all of the garnet clinopyroxenites had deformed under the same stress conditions, the relationship shown in Fig. 18a suggests that garnet-dominated part has been more strained than clinopyroxene-diminated part. However, the results of an experimental study performed at high temperature and pressure (1500 K, 3 GPa) revealed that garnet is three to four times as strong as omphacite (Jin *et al*., 2001).

The olivine fabrics measured in the present study suggest that the garnet clinopyroxenites were plastically sheared under wet conditions, and FTIR analyses reveal H_2O contents in garnet of 17–1000 ppm (mostly ~60 ppm; Fig. 11; Table 4). It is possible that the presence of water influences the deformation of garnet. Indeed, Katayama and Karato (2008) reported that the creep rate of Mg-rich garnet ($Alm_{19}Prp_{68}Grs_{12}$) is sensitive to water. Figure 22 shows the relation between stress and strain rate for garnet and diopside under dry and wet conditions. Here, the water contents of wet and dry garnet are

80–200 ppm and < 30 ppm, respectively (Katayama and Karato, 2008). The results reveal contrasting influences of water on the deformation of garnet and diopside: under wet conditions compared with dry, the strain rate increases by two orders of magnitude for garnet but by an order of magnitude for diopside. Given the influence of water on the creep strength of garnet, garnet within the Higashi-akaishi mass may have become significantly as weak as clinopyroxene during deformation. It should be, however, noted that the creep strength of minerals may be also influenced by some other effects such as stress or pressure as well as the effect of water (e.g., Chen et al., 2006; Li et al., 2006; Katayama and Karato, 2008; Amiguet et al., 2009).

8.5. Implications for the deformation of deeply subducted slabs

The rheological behavior of garnet is an important factor in the deformation of subducted oceanic crust, as oceanic crust that has been deeply subducted (> 400 km depth) is composed largely of garnet (Ringwood, 1982). The nominally anhydrous mineral phases (NAMs; olivine, pyroxene, and garnet) in both subducting oceanic crust and the overlying mantle wedge can carry a significant amount of H_2O to the deep mantle (Forneris and Holloway, 2003; Iwamori, 2007). If water has a stronger influence on the creep strength of garnet than on that of clinopyroxene, as shown above, oceanic crust would be expected to weaken with ongoing subduction. This hypothesis is the opposite to that suggested in previous studies (e.g., Karato *et al*., 1995; Jin *et al*., 2001) and may have implications for our understanding of mantle convection.

9. Conclusion

Dunites in the Higashi-akaishi peridotite mass, located in the subduction-type Sanbagawa metamorphic belt, record two stages of deformation (D1 and D2; Mizukami and Wallis, 2005) and contain various microstructures, ranging from coarse-grained to porphyroclastic. At Gongen Pass, dunites contain fine-grained textures with weak fabric strength, suggesting that the outcrop represents the center of a D2 shear zone. CPO patterns for olivine are B-type regardless of texture. Accordingly, dunite within the Higashi-akaishi mass is interpreted to have been deformed under high-stress and wet conditions.

Garnet clinopyroxenites that occur within foliated dunite at Gongen Pass contain 3–80% garnet, and garnet and clinopyroxene within these rocks have a homogeneous

distribution. Garnet contains extensive, regular dislocation arrays and dislocation networks, suggesting that dislocation creep was the dominant deformation mechanism. Analyses of orientation maps reveal that garnet and clinopyroxene have similar grain sizes and aspect ratios, regardless of modal composition. These findings indicate that the two minerals were deformed under similar conditions of plasticity. In addition, *M*-index values for both garnet and clinopyroxene increase with increasing modal composition of garnet. During deformation, garnet was possibly weaker than clinopyroxene. The obtained olivine CPOs indicate deformation under wet conditions, and the water content of garnet is ~60 ppm. It is possible that the presence of water helped to induce garnet deformation, and flow laws indicate that under water-rich conditions (relative to dry conditions), the strain rate for garnet increases by two orders of magnitude, whereas for diopside it increases by an order of magnitude. This finding may have significant implications for our understanding of mantle convection, as garnet may in fact be weaker than clinopyroxene.

Acknowledgements

The authors thank ~~Hiroyuki Kagi of University of Tokyo for assistance with FTIR analyses and~~ M. Satish-Kumar of Shizuoka University for assistance with EPMA analyses. We would like to thank Toshiaki Masuda of Shizuoka University for help in using the Ion thinning technique, and Yasuro Kugimiya for providing samples for analysis. MM wishes to thank Takumi Nanbu, Masahiro Hara, Kyoko Kanayama, and members of the Michibayashi Laboratory (Yumiko Harigane, Takako Satsukawa, Hisashi Imoto, Ayano Fujii, Shigeki Uehara, Tatsuya Ohara, Makoto Suzuki, Naohiko Ueta, Naoaki Komori, and Yuri Shinkai) for their helpful advice and discussions.

References

Amiguet, E., Raterron, P., Cordier, P., Couvy, H. and Chen, J., 2009. Deformation of diopside single crystal at mantle pressure, 1, Mechanical data. *Physics of the Earth and Planetary Interiors*, **177**, 122-129.

Ando, J., Fujino, K. and Takeshita, T., 1993. Dislocation microstructures in naturally deformed silicate garnets. *Physics of the Earth and Planetary Interiors*, **80**, 105-116.

Aoya, M., 2001. P-T-D path of eclogite from the Sambagawa belt deduced from combination of petrological and microstructural analyses. *Journal of Petrology*, **42**, 1225–1248.

Ave Lallemant, H. G., 1978. Experimental deformation of diopside and websterite. *Tectonophysics*, **48**, 1–27.

Bascou, J., Tommasi, A. and Mainprice, D., 2002. Plastic deformation and development of clinopyroxene lattice preferred orientations in eclogites. *Journal of Structural Geology*, **24**, 1357–1368.

Bell, D. R. and Rossman, G. R., 1992. The distribution of hydroxyl in garnets from the subcontinental mantle of southern Africa. *Contributions to Mineralogy and Petrology*, **111**, 161-178.

Bell, D. R., Ihinger, P. D. and Rossman, G. R., 1995. Quantitative analysis of hydroxyl in garnet and pyroxene. *American Mineralogist*, **80**, 465-474.

Bestmann, M., Habler, G., Heidelbach, F. and Thoni, M., 2008. Dynamic recrystallization of garnet and related diffusion processes. *Journal of Structural Geology*, **30**, 777–790

Bunge, H. J., 1982. *Texture Analysis in Materials Sciences*. 593p., Buttleworth, London.

Bystricky, M. and Mackwell, S., 2001. Creep of dry clinopyroxene aggregates. *Journal of Geophysical Research*, **106**, 13443-13454.

Chen, S., Hiraga, T. and Kohlstedt, D. L., 2006. Water weakening of clinopyroxene in the dislocation creep regime. *Journal of Geophysical Research*, **111**, B08203, doi:10,1029/2005JB003885.

Dalziel, I. W. and Bailey, S. W., 1968. Deformed garnets in a mylonitic rock from the grenville front and their tectonic significance. *American Journal of Science*, **266**, 542-562.

Doukhan, N., Sautter, V. and Doukhan, J. C., 1994. Ultradeep, ultra-mafic mantle xenoliths – transmission electron microscopy preliminary results. *Physics of the Earth and Planetary Interiors*, **82**, 195–207.

Enami, M., 1983. Petrology of pelitic schists in the oligoclase-biotite zone of the Sanbagawa metamorphic terrain, Japan: phase equilibria in the highest grade zone of a high-pressure intermediate type of metamorphic belt. *Journal of Metamorphic Geology*, **1**, 141–161.

Enami, M., Wallis, S. R. and Banno, Y., 1994. Paragenesis of sodic pyroxene-bearing quartz schists: implications for the P-T history of the Sanbagawa belt. *Contributions to Mineralogy and Petrology*, **116**, 182–198.

Enami, M., Mizukami, T. and Yokoyama, K., 2004. Metamorphic evolution of garnet-bearing ultramafic rocks from the Gongen area, Sanbagawa belt, Japan. *Journal of Metamorphic Geology*, **22**, 1-15.

Forneris, J. F. and Holloway, J. R., 2003. Phase equilibria in subducting basaltic crust: implications for H_2O release from the slab. *Earth and Planetary Science Letters*, **214**, 187–201.

Godard, G. and van Roermund, H. L. M., 1995. Deformation-induced clinopyroxene fabrics from eclogites. *Journal of Structural Geology*, **17**, 1425-1443.

Higashino, T., 1990. The higher grade metamorphic zonation of the Sambagawa metamorphic belt in central Shikoku, Japan. *Journal of Metamorphic Geology*, **8**, 413-423.

Holtzman, B. K., Kohlstedt, D. L., Zimmerman, M. E., Heidelbach, F., Hiraga, T. and Hustoft, J., 2003. Melt segregation and strain partitioning: implications for seismic anisotropy and mantle flow. *Science*, **301**, 1227–1230.

Horikoshi, G., 1937. On the eclogite in the vicinity of Higashiakaishi- yama in the province of Iyo. *Journal of Geological Society of Japan*, **44**, 141–144 (in Japanese).

Ji, S. C. and Martignole, J., 1994. Ductility of garnet as an indicator of extremely high temperature deformation. *Journal of Structural Geology*, **16**, 985-996.

Ji, S. C., Saruwatari, K., Mainprice, D., Wirth, R., Xu, Z. and Xia, B., 2003. Microstructures, petrofabrics and seismic properties of ultra high pressure eclogites from Sulu region, China: implications for rheology of subducted continental crust and origin of mantle reflections. *Tectonophysics*, **370**, 49–76.

Ji, S. C., Zhao, P. and Saruwatari, K., 1997. Fracturing of garnet crystals in anisotropic metamorphic rocks during uplift. *Journal of Structural Geology*, **19**, 603– 620.

Jin, Z. M., Zhang, J., Green II, H. W. and Jin, S., 2001. Eclogite rheology: implications for subducted lithosphere. *Geology*, **29**, 667– 670.

Jung, H. and Karato, S., 2001a, Water-induced fabric transitions in olivine. *Science*, **293**, 1460–1463.

Jung, H. and Karato, S., 2001b. Effect of water on dynamically recrystallized grain-size of olivine. *Journal of Structural Geology*, **23**, 1337-1344.

Iwamori, H., 2007. Transportation of H2O beneath the Japan arcs and its implications for global water circulation. *Chemical Geology*, **239,** 182–198.

Karato, S., Wang, Z. C., Liu, B. and Fujino, K., 1995. Plastic deformation of garnets: systematic and implications for the rheology of the mantle transition zone. *Earth and Planetary Science Letters*, **130**, 13-30.

Katayama, I. and Karato, S., 2008. Effects of water and iron content on the rheological contrast between garnet and olivine. *Physics of the Earth and Planetary Interiors*, **166**, 57–66.

Kleinschrodt, R. and McGrew, A.J., 2000. Garnet plasticity in the lower continental crust: implications for deformation mechanisms based on microstructures and SEM electron channeling pattern analysis. *Journal of Structural Geology*, **22**, 795–809.

Li, L., Long, H., Raterron, P. and Weidner, D., 2006. Plastic flow of pyrope at mantle pressure and temperature, *American Mineralogist*, **91**, 517-525.

Mainprice, D., Bascou, J., Cordier P. and Tommasi A., 2004. Crystal preferred orientations of garnet: comparison between numerical simulations and electron back-scattered diffraction (EBSD) measurements in naturally deformed eclogites. *Journal of Structural Geology*, **26**, 2089-2102

Mercier, J-C. C. and Nicolas, A., 1975. Textures and fabrics of upper-mantle Peridotites as illustrated by xenoliths from basalts. *Journal of Petrology*, **16**, 454-487.

Michibayashi, K., 1993. Syntectonic development of a strain independent dynamically recrystallized quartz grain during mylonitization. *Tectonophysics*, **222**, 151–164.

Michibayashi, K. and Mainprice, D., 2004. The role of pre-existing mechanical anisotropy on shear zone development within oceanic mantle lithosphere: an example from the Oman ophiolite. *Journal of Petrology*, **45**, 405–414.

Michibayashi, K. and Masuda, T., 1993. Shearing during progressive retrogression in granitoids: abrupt grain size reduction of quartz at the plastic–brittle transition for feldspar. *Journal of Structural Geology*, **15**, 1421–1432.

Michibayashi, K., Okamoto, A., Masuzawa, T., Kawakami, T., Ikeda, T. and Yasuda, H., 2004. Orientation contrast images of garnet from granulite quartzite, Lutzow-Holm Complex, East Antarctica. *The Journal of the Geological Society of Japan*. **110**, 5–6.

Michibayashi, K., Ina, T. and Kanagawa, K., 2006. The effect of dynamic recrystallization on olivine fabric and seismic anisotropy: insight from a ductile shear zone, Oman ophiolite. *Earth and Planetary Science Letters*, **244**, 695–708.

Miyashiro, A., 1961. Evolution of metamorphic belts. *Journal of Petrology*, **2**, 277–331.

Mizukami, T. and Wallis, S. R., 2005. Structural and petrological constraints on the tectonic evolution of the garnet-lherzolite facies Higashi-akaishi peridotite body, Sanbagawa belt, SW Japan. *Tectonics*, **24**, 1-17.

Mizukami, T., Wallis, S. R. and Yamamoto, J., 2004. Natural example of olivine lattice preferred orientation patterns with a flow-normal a-axis maximum. *Nature*, **427**, 29.

Mori, T. and Banno, S., 1973. Petrology of peridotite and garnet clinopyroxenite of the Mt. Higashi-Akaishi mass, Central Shikoku, Japan – Subsolidus relation of anhydrous phases. *Contributions to Mineralogy and Petrology*, **41**, 301–323.

Nicolas, A., Boudier, F. and Boullier, A. M., 1973. Mechanism of flow in naturally and experimentally deformed peridotites. *American Journal of Science*, **273**, 853–876.

Okamoto, A. and Michibayashi, K., 2005. Progressive shape evolution of a mineral inclusion under differential stress at high temperature: example of garnet inclusions within a granulite facies from the Lutow–Holm complex, East Antarctica. *Journal of Geophysical Research*, **110**, B11203. doi:10.1029/2004JB003526.

Orzol, J., Stockhert, B., Trepmann, C. A. and Rummel, F., 2006. Experimental deformation of synthetic wet jadeite aggregates. *Journal of Geophysical Research*, **111**, B06205, doi:10.1029/2005JB003706.

Passchier, C. W. and Simpson, C., 1986. Porphyroclast systems as kinematic indicators. *Journal of Structural Geology*, **8**, 831–843.

Prior, D. J., Wheeler, J., Brenker, F. E., Harte, B. and Matthews, M., 2000. Crystal plasticity of natural garnet: new microstructural evidence. *Geology*, **28**, 1003–1006.

Ringwood, A.E., 1982. Phase transformation and differentiation in subducted lithosphere: Implications for mantle dynamics, basalt petrogenesis, and crustal evolution. *Journal of Geology*, **90**, 611–643.

Rossman, G. R. and Smyth, J. R., 1990. Hydroxyl contents of accessory minerals in mantle eclogites and related rocks. *American Mineralogist*, **75**, 775-780.

Skemer, P., Katayama, I. and Karato, S., 2005. The misorientation index: Development of a new method for calculating the strength of lattice-preferred orientation. *Tectonophysics*, 411, 157–167.

Stipp, M., Stunitz, H., Heilbronner, R. and Schmid, S. M., 2002. The eastern Tonale fault zone: a 'natural laboratory' for crystal plastic deformation of quartz over a temperature range from 250 to 700℃. *Journal of Structural Geology*, **24**, 1861-1884.

Storey, G. D. and Prior, D. J., 2005. Plastic deformation and recrystallization of garnet: a mechanism to facilitate diffusion creep. *Journal of petrology*, **46**, 2593–2613.

Takasu, A., 1989. P-T histories of peridotite and amphibolite tectonic blocks in the Sanbagawa metamorphic belt, Japan, Evolution of Metamorphic Belts. *Geological Society Publication*, **43**, 533-538.

Tasaka, M., Michibayashi, K. and Mainprice, D., 2008. B-type olivine fabrics developed in the fore-arc side of the mantle wedge along a subducting slab. *Earth and Planetary Science Letters*, **272**, 747–757.

Terry, M. P. and Heidelbach, F., 2004. Superplasticity in garnet from eclogite facies shear zones in the Haram Gebbro, Haramsøya, Norway. *Geology*, **32**, 281–284.

Tommasi, A., Tikoff, B. and Vauchez, A., 1999. Upper mantle tectonics: three-dimensional deformation, olivine crystallographic fabrics and seismic properties. *Earth and Planetary Science Letters*, **168**, 173–186.

Tommasi, A., Mainprice, D., Canova, G. and Chastel, Y., 2000. Viscoplastic self-consistent and equilibrium-based modeling of olivine lattice preferred orientations: implications for the upper mantle seismic anisotropy. *Journal of Geophysical Research*, **105**, 7893–7908.

Van der Wal, D., Chopra, P., Drury, M. R. and Fitzgerald, J. D., 1993. Relationships between dynamically recrystallized grain size and deformation conditions in experimentally deformed olivine rocks. *Geophysical Research Letters*, **20**, 1479–1482.

Voegelé, V., Cordier, P., Sautter, V., Sharp, T. G., Lardeaux, J. M. and Marques, F. O., 1998. Plastic deformation of silicate garnets II.Deformation microstructure in natural samples. *Physics of Earth and Planetary Interior*, **108**, 319-338.

Wallis, S. and Aoya, M., 2000. A re-evaluation of eclogite facies metamorphism in SW Japan: Proposal for an eclogite nappe. *Journal of Metamorphic Geology*, **18**, 653–664.

Wallis, S., Takasu, A., Enami, M. and Tsujimori, T., 2000. Eclogite and related metamorphism in the Sanbagawa belts, Southwest Japan. *Bulletin of Research Institute of Natural Sciences, Okayama University of Science*, **26**, 3–17.

Wang, Z. C. and Ji, S. C., 1999. Deformation of silicate garnets: brittle ductile transition and its geological implications. *Canadian Mineralogist*. **37**, 525–541.

Zhang, J. and Green, H. W., 2007. Experimental investigation of eclogite rheology and its fabrics at high temperature and pressure. *Journal of Metamorphic Geology*, **25**, 97–115.

Figure(s)
Click here to download Figure(s): Muramoto_figures.doc

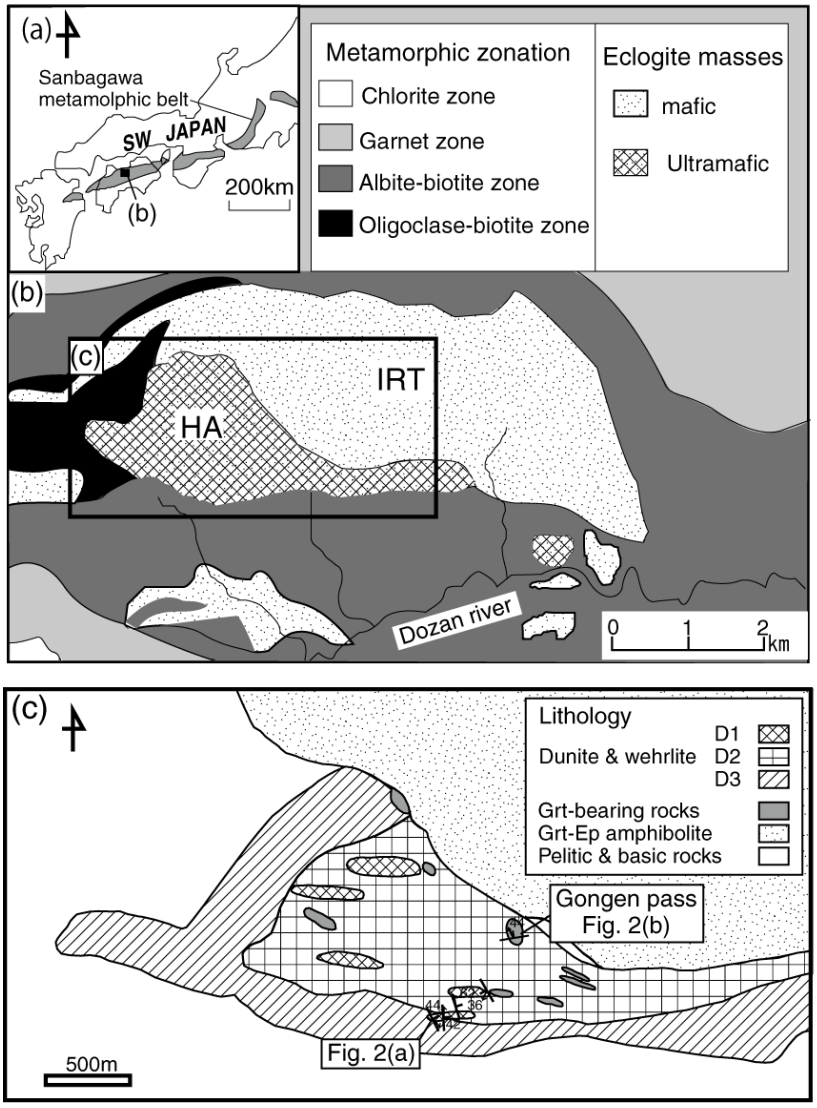

Figure 1. Geological maps of the (a) South west Japan, and (b) Besshi region (partly modified from Aoya, 2001). Abbreviations are: HA, Higashi-akaishi peridotite mass; IRT, Iratsu mass. (c) Geological map and distributions of D1, D2, and D3 fabrics (Mizukami & Wallis, 2005) in the Higashi-akaishi peridotite mass.

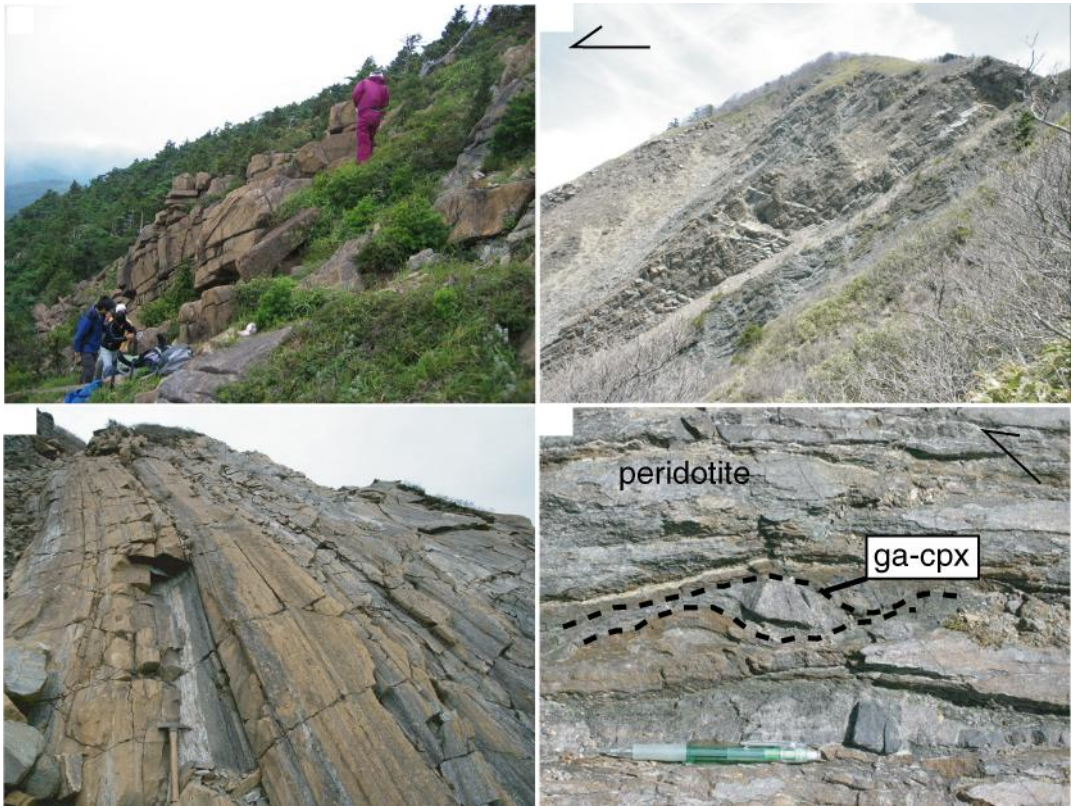

Figure 2. Photographs showing outcrops of the Higashi-akaishi peridotite mass.(a) Massive dunites around top of the Mt.Higashi-akaishi. (b), (c), (d) Foliated dunite at Gongen pass. (b) Length of the outcrop is about 100m. (c) Strong liniation of foliated dunite (Mullion structure). scale is the hammer (~ 30 cm).(d) Garnet clinopyroxenite lens (ga-cpx) in the foliated dunite.

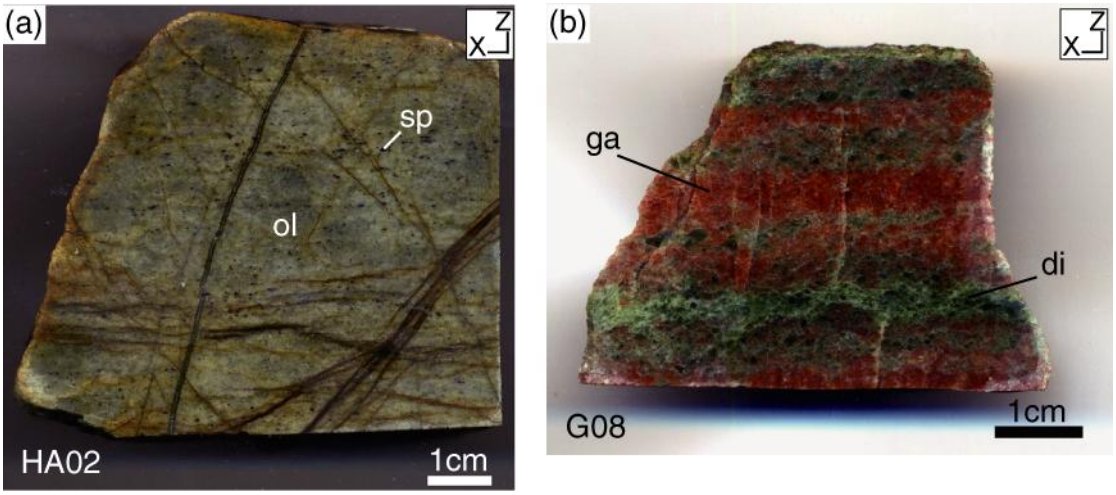

Figure 3. Photographs of polished (a) peridotite and (b) garnet clinopyroxenite. Ol, olivine; sp, spinel; ga, garnet; di, diopside.

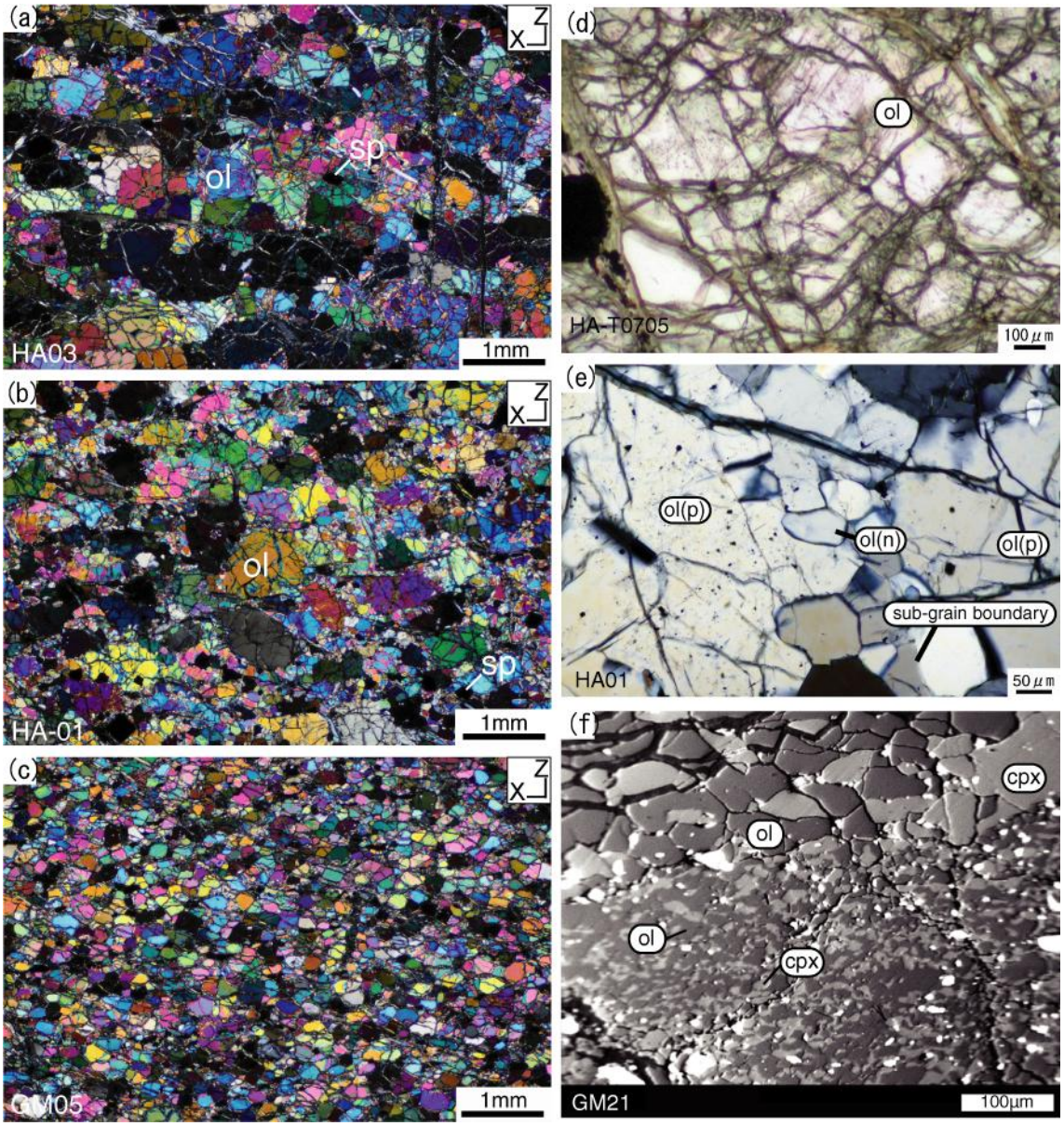

Figure 4. Photomicrographs of Higashi-akaishi peridotites. ol, olivine; sp, spinel; cpx, clinopyroxene. ol(p), olivine porphyroclast; ol(n), olivine neoblast. (a) Coarse-grained texture of dunite. (b) Porphyroclastic texture of dunite. (c) Fine-grained texture of dunite at Gongen pass. (d) Olivine of coarse-grained texture have many microinclusions. (e) Clear neoblasts of olivine formed at the center of dusty olivine porphyroclast. These neoblasts are closely associated with a subgrain boundary within the porphyroclast. (f) Ultra fine-grained zone (COMP image). Grain size is about 20 μm. Cpx occurs only this layer.

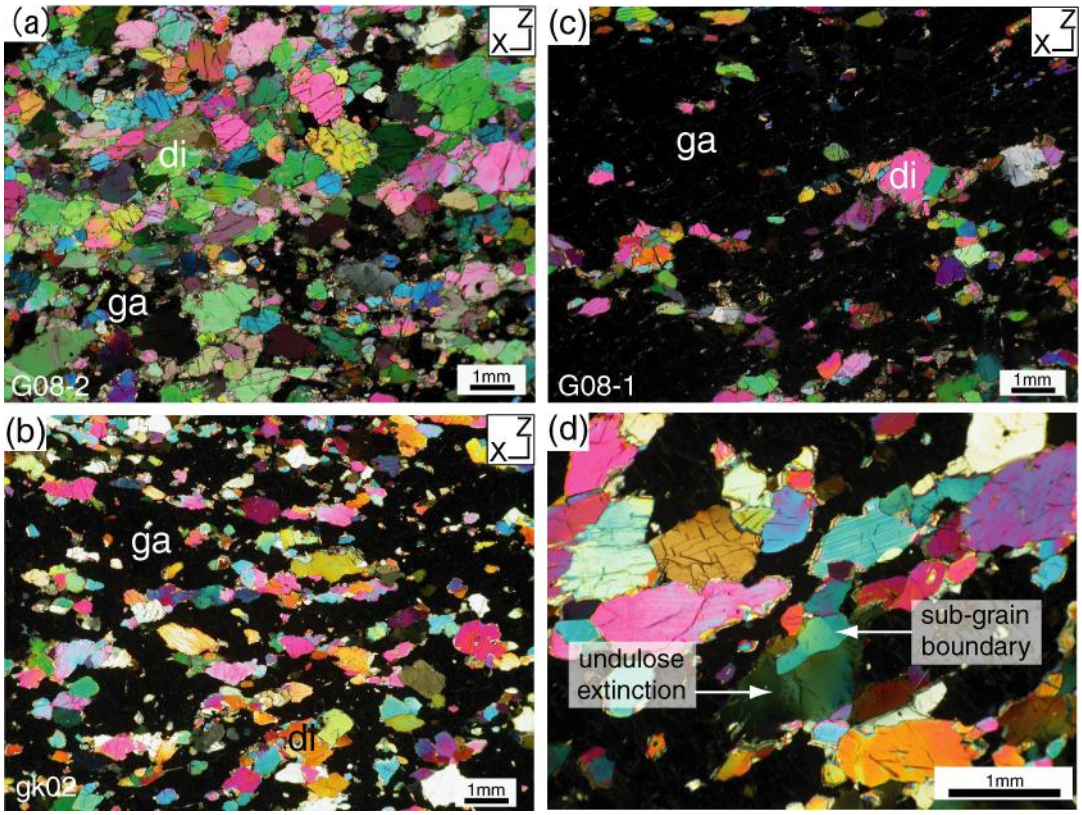

Figure 5. Photomicrographs of Higashi-akaishi garnet clinopyroxenites. ga, garnet; di, diopside. (a) and (c) are different regions in same sample. (a) Modal composition; garnet, 29% , diopside, 71%. (b) Garnet, 55%; Diopside, 45%. (c) Garnet, 81%; Diopside, 19%. (d) Deformation microstructures of diopside.

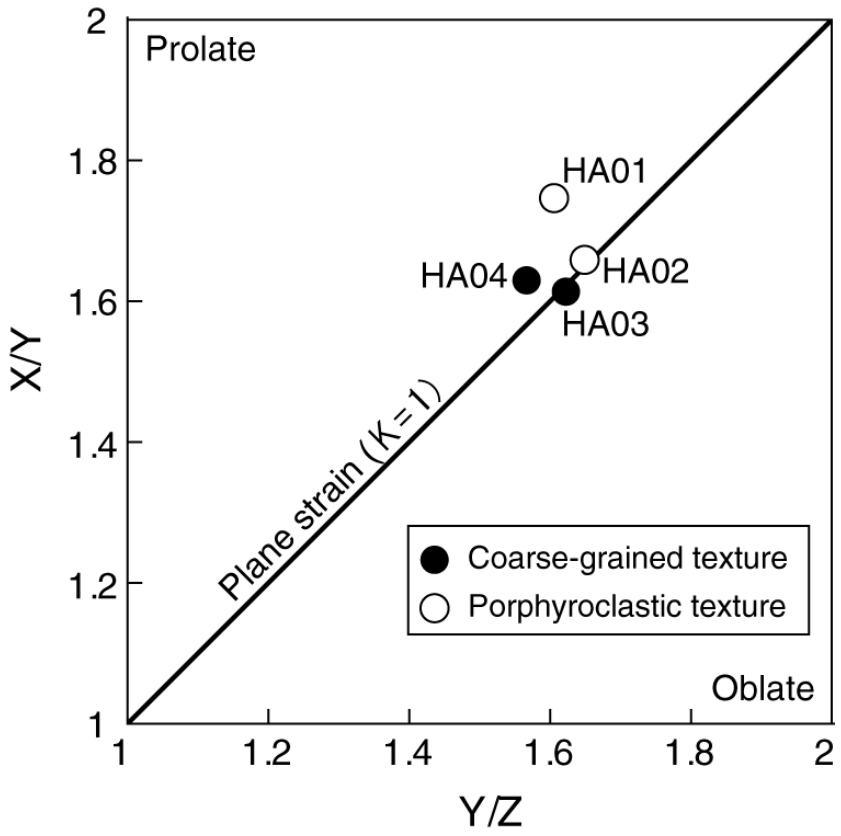

Figure 6. Flinn plot of peridotites. Solid circle is coarse-grained texture. Open circle is Porphyroclastic texture. X, Y and Z are the mean crystal lengths in the directions parallel to the stretching lineation, perpendicular to the stretching lineation and in the foliation plane and normal to the foliation, respectively.

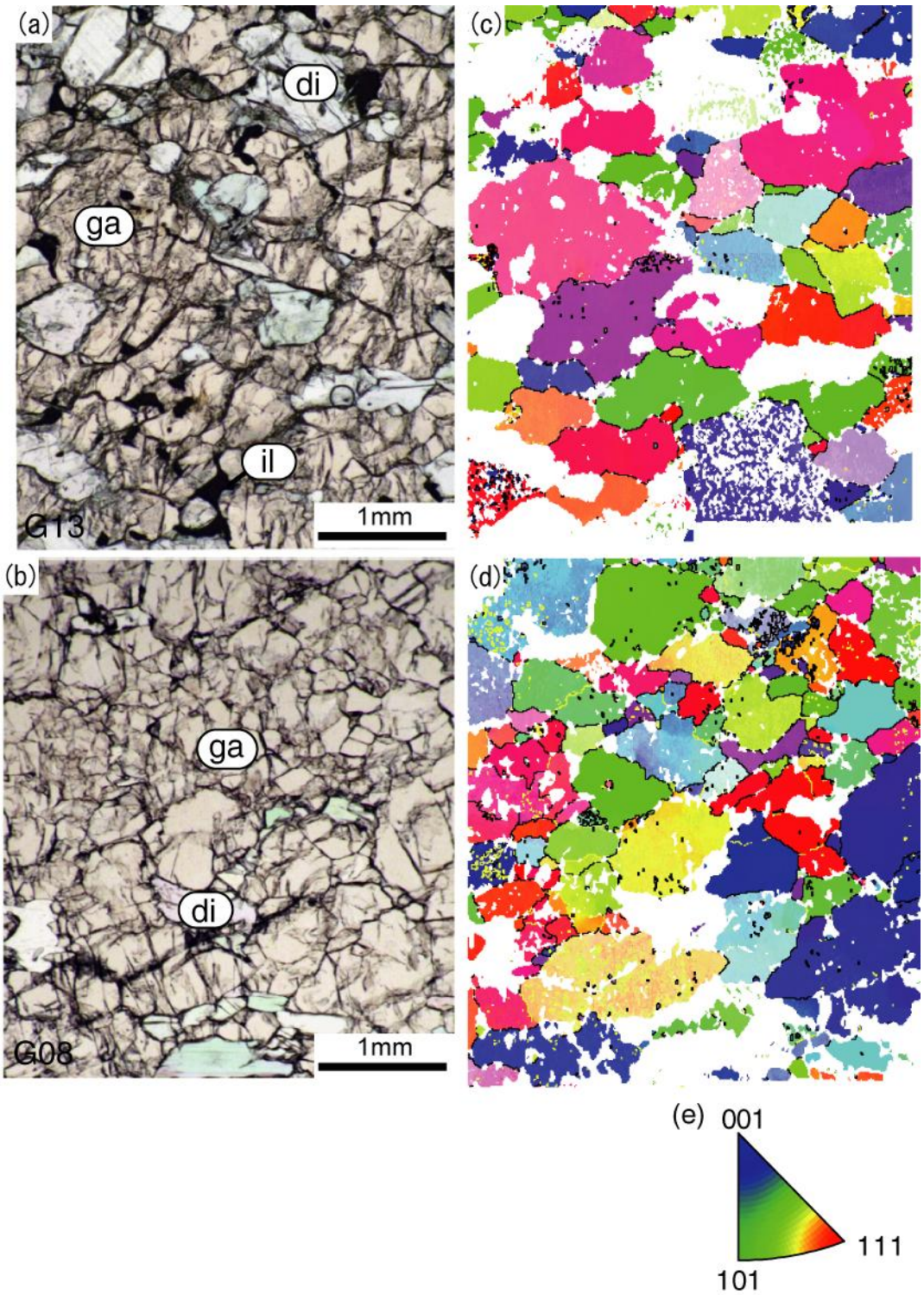

Figure 7. Orientation maps of garnet. Optical microphotograph of Garnet clinopyroxenites (a, b) and Crystal-preferred orientation maps of garnet at same place (c, d). ga: garnet, di: diopside, il: ilmenite. (f) Inverse pole figure (IPF) color map. Orientation maps are painted inverse pole figure (IPF) color.Black lines are drawn between any two adjacent points with a misorientation >10°. Yellow lines: 2-9°

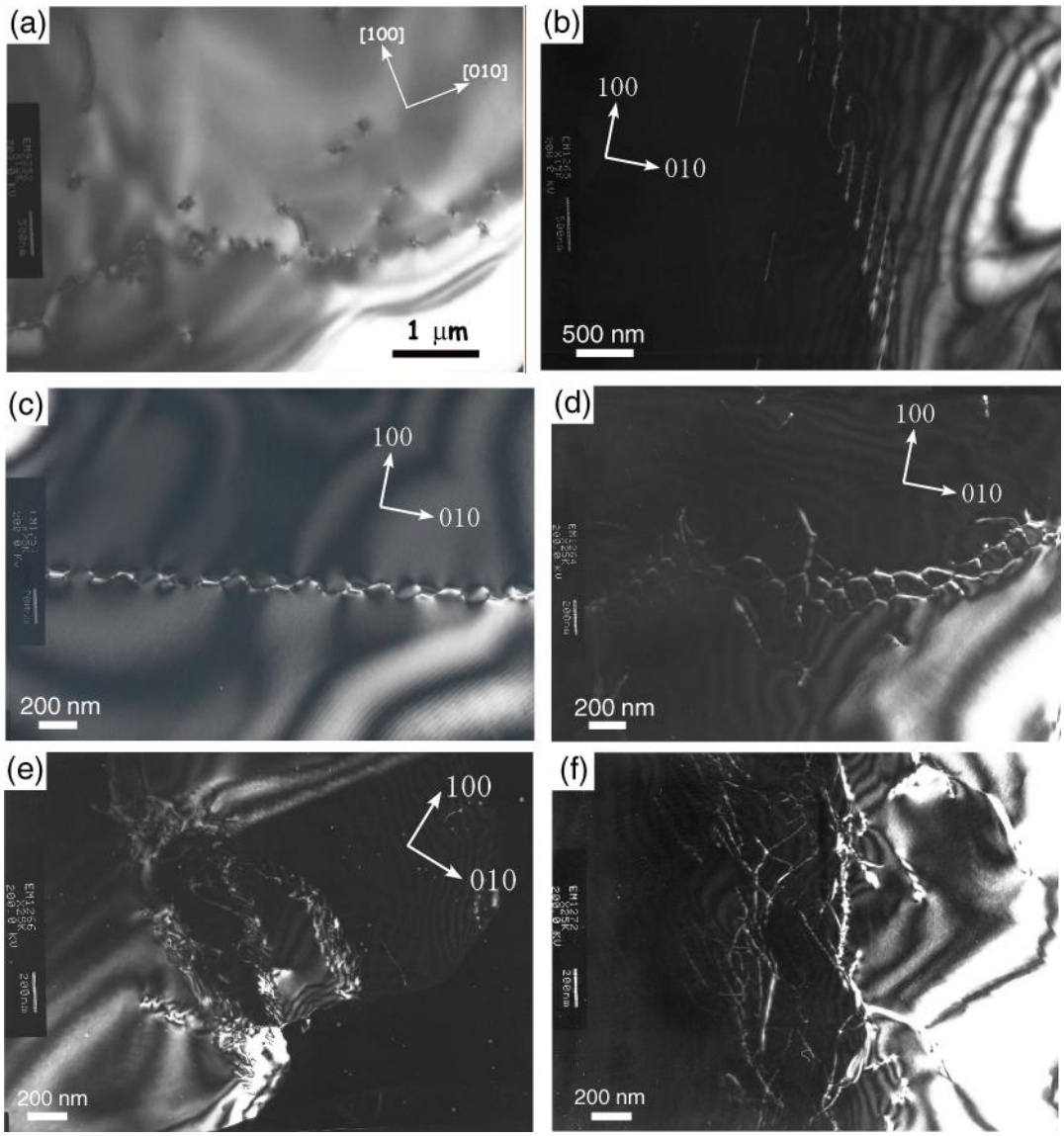

Figure 8. TEM microphotographs of garnet grains. (a) Bright field image (sample: G08). (b-f)Dark field image(sample: GM01).(a)Dislocation walls defined by well-organized and free-dislocations (sample:G08). (b) Dislocation walls. Linear array of straight dislocations. (c, d) Dislocation networks defined by polygonal array of dislocations of three discrete orientations. (e) Subgrain surrounded by dislocation walls. (f) Dislocation junctions.

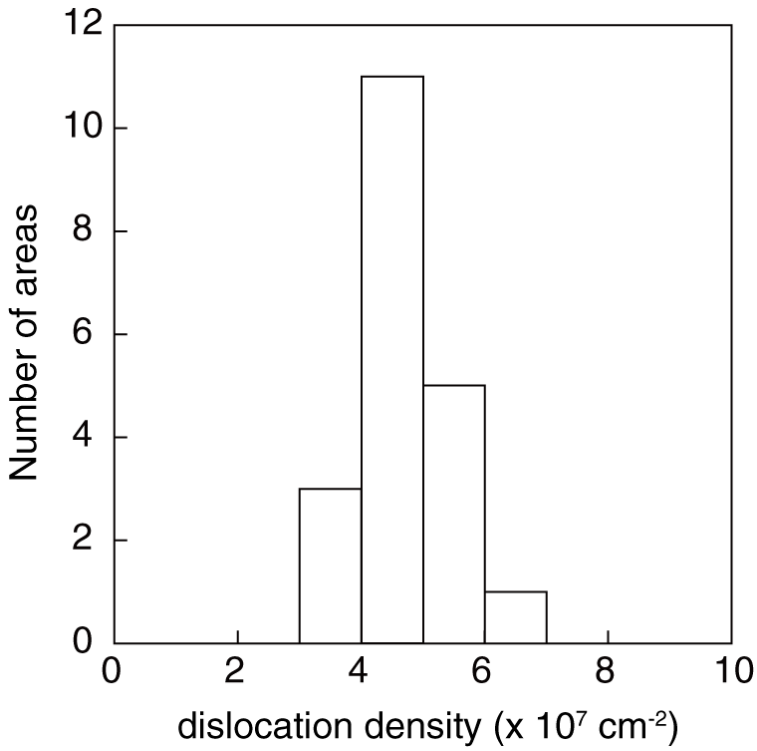

Figure 9. Dislocation density of garnet (GM01). A measured area is about 20x20μm.

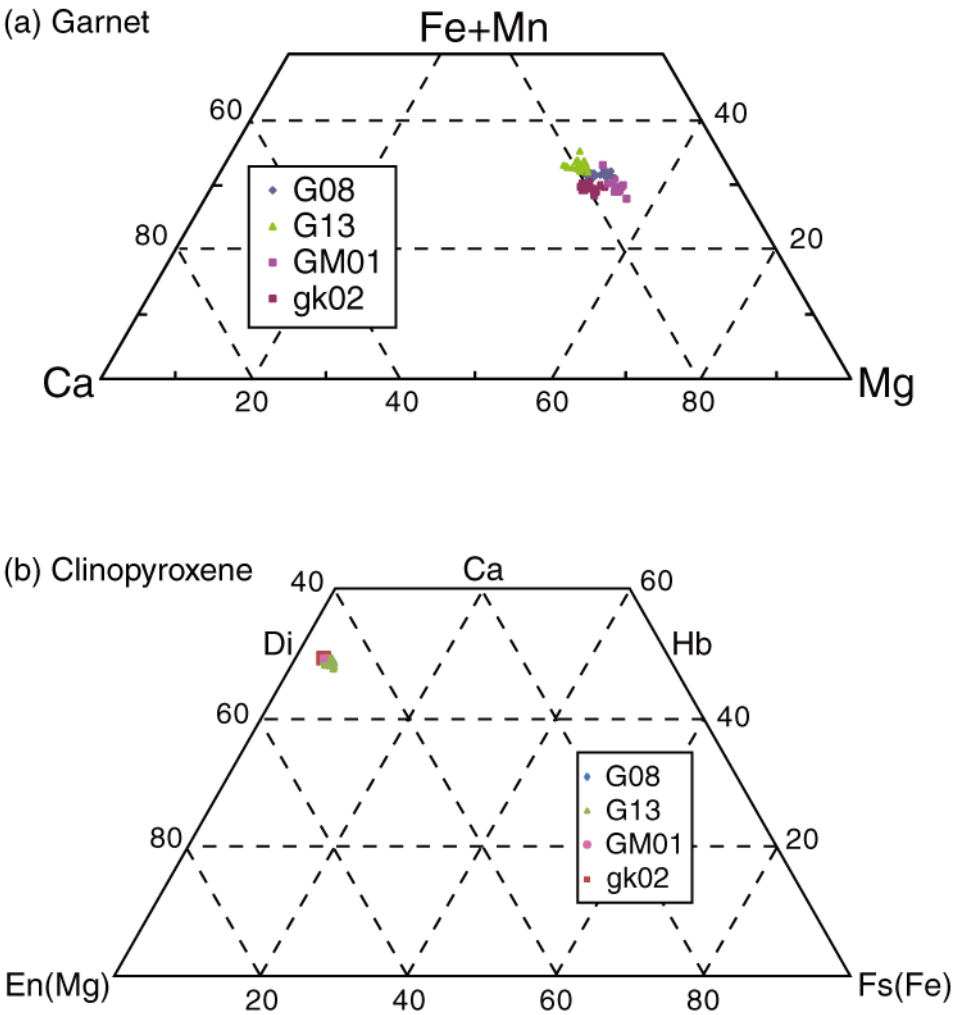

Figure 10. Chemical compositions of garnet (a) and clinopyroxene (b).

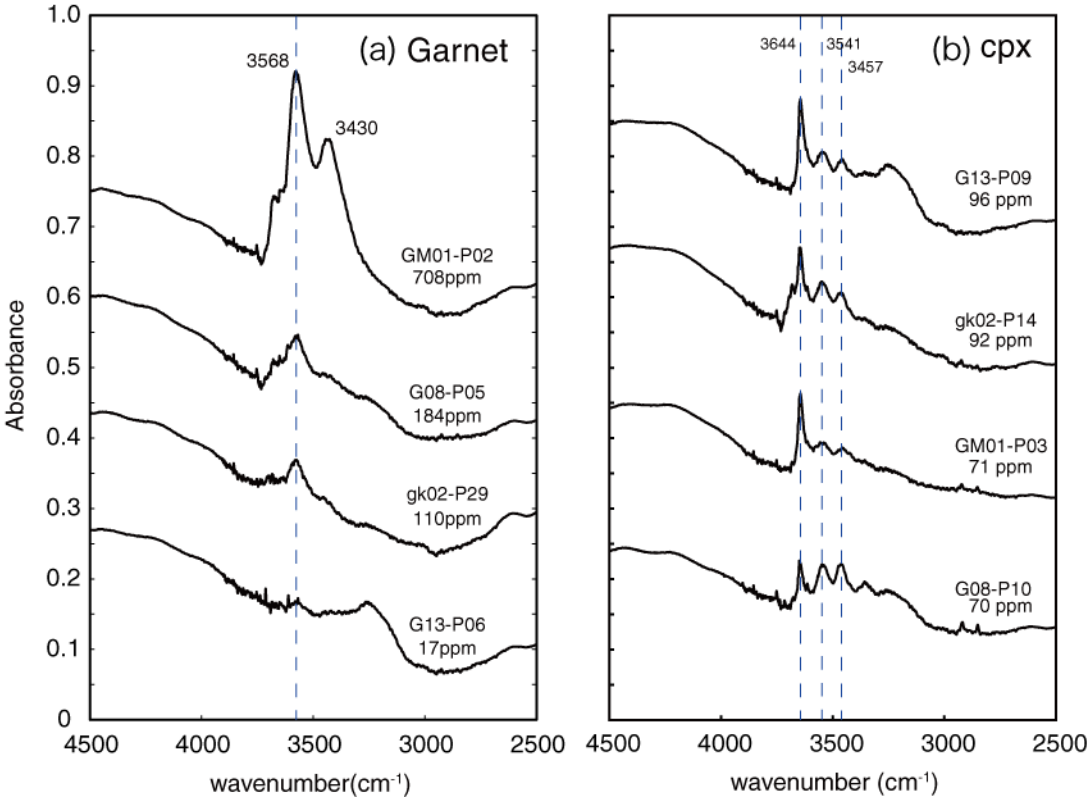

Figure 11. FTIR spectra of garnet (a) and clinopyroxene (b). (a) The 3570 cm-1 peak is from structural OH in the garnets. (b) The 3460, 3540 and 3640 cm−1 peaks are from structural OH in the clinopyroxene

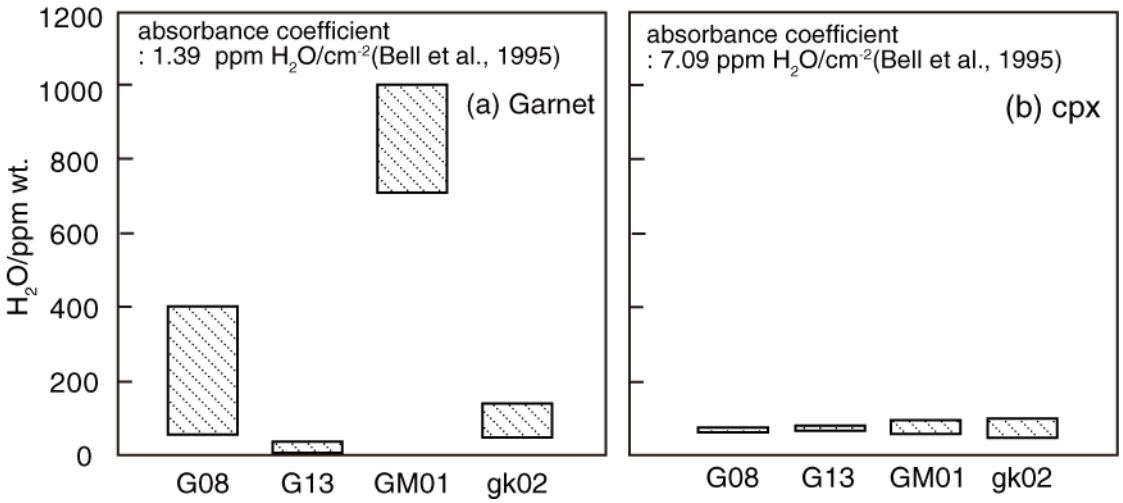

Figure 12. Water contents of garnet (a) and clinopyroxene (b). Absorbance coefficients are 1.39 for garnet and 7.09 for clinopyroxene.

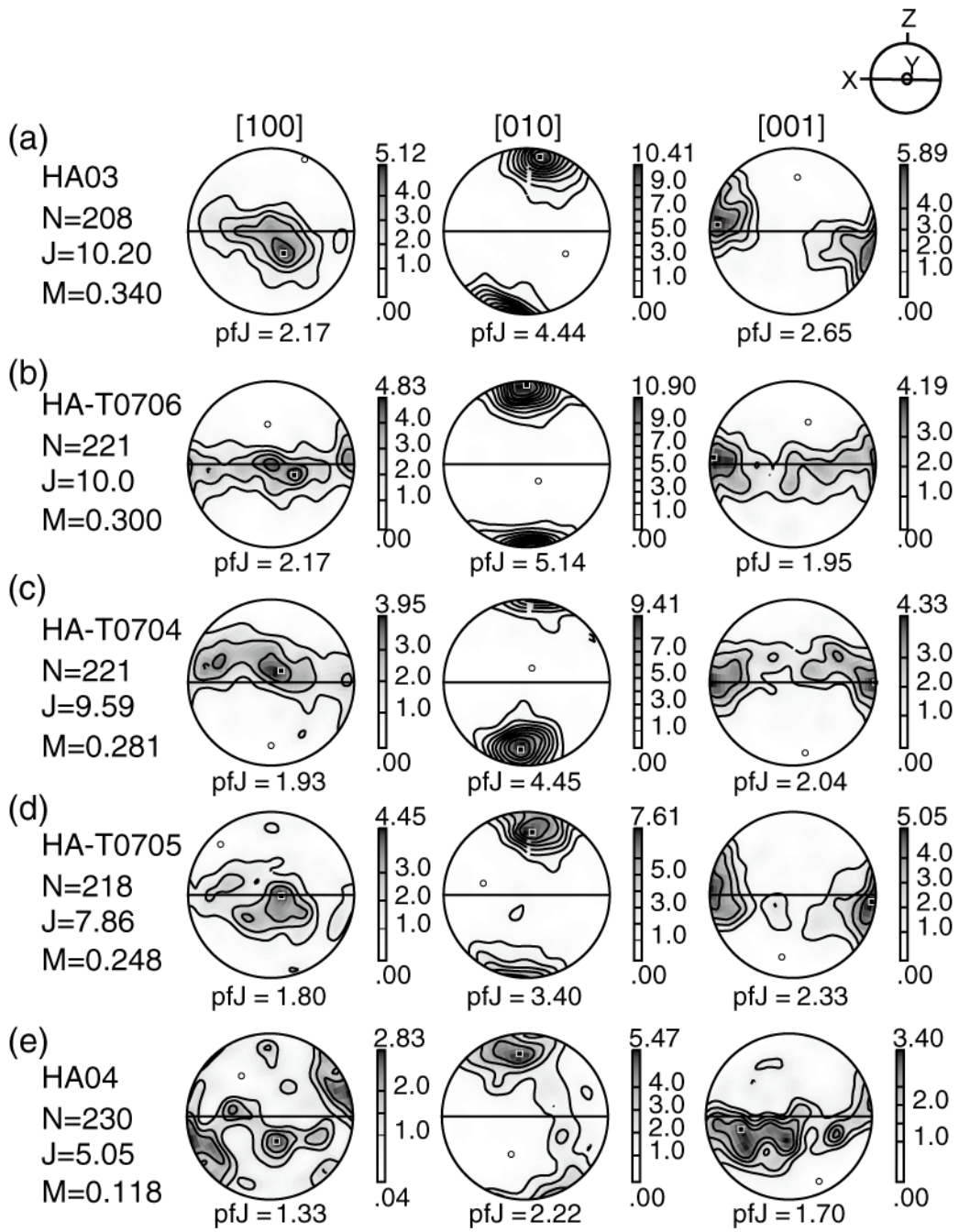

Figure 13. Olivine CPO data of Coarse-grained texture. Equal area, lower hemisphere projections. Contours are multiples of uniform distribution. Foliation (XY) is horizontal and lineation (X) is E–W. N is number of measuring point. *J*, *M* and *pfJ* are the fabric intensities calculated after Mainprice et al. (2000), Michibayashi and Mainprice (2004) and Skemer et al. (2005).

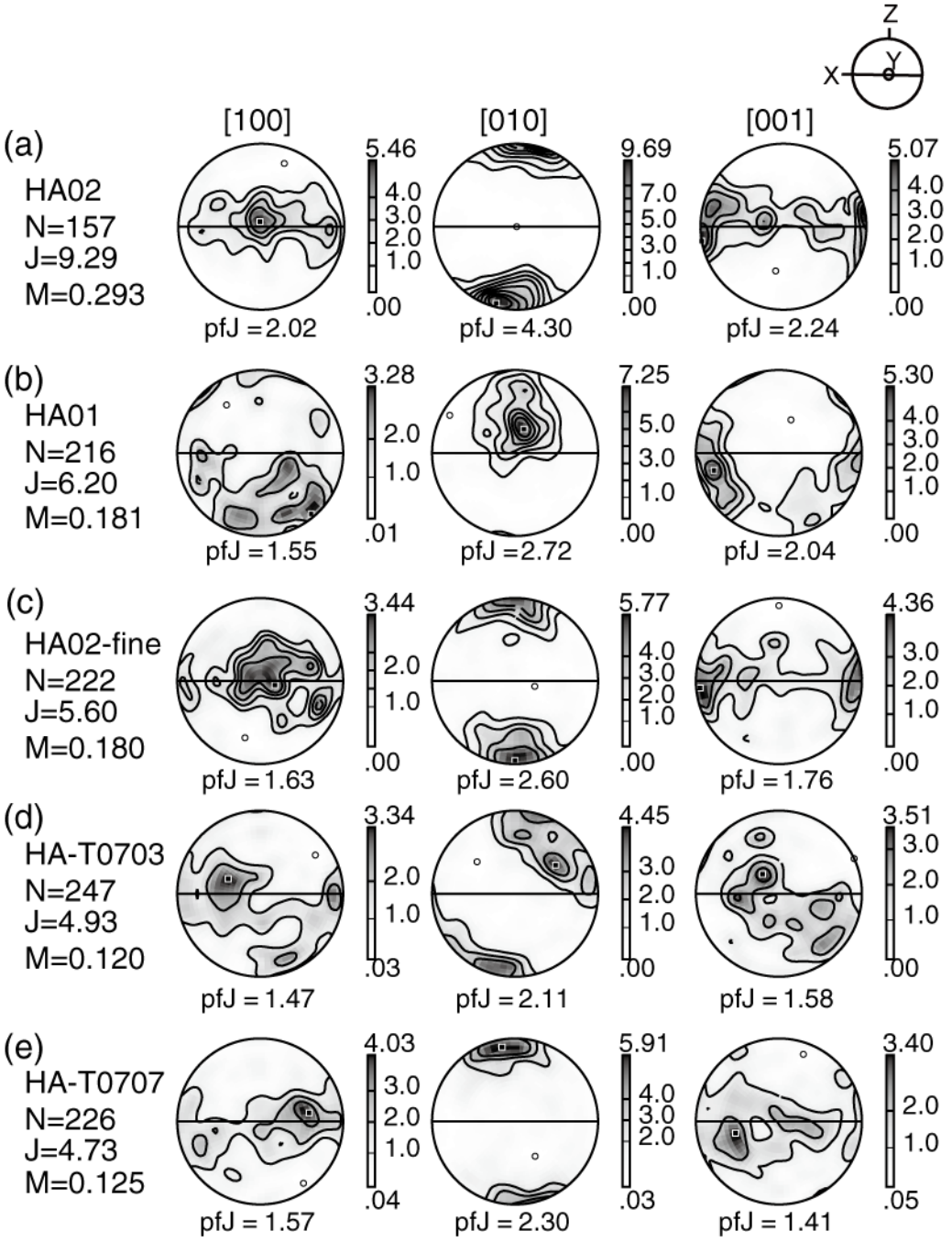

Figure 14. Olivine CPO data of Porphyroclastic texture. (a) and (c) represent porphyroclasts and neoblasts within HA02, respectively.

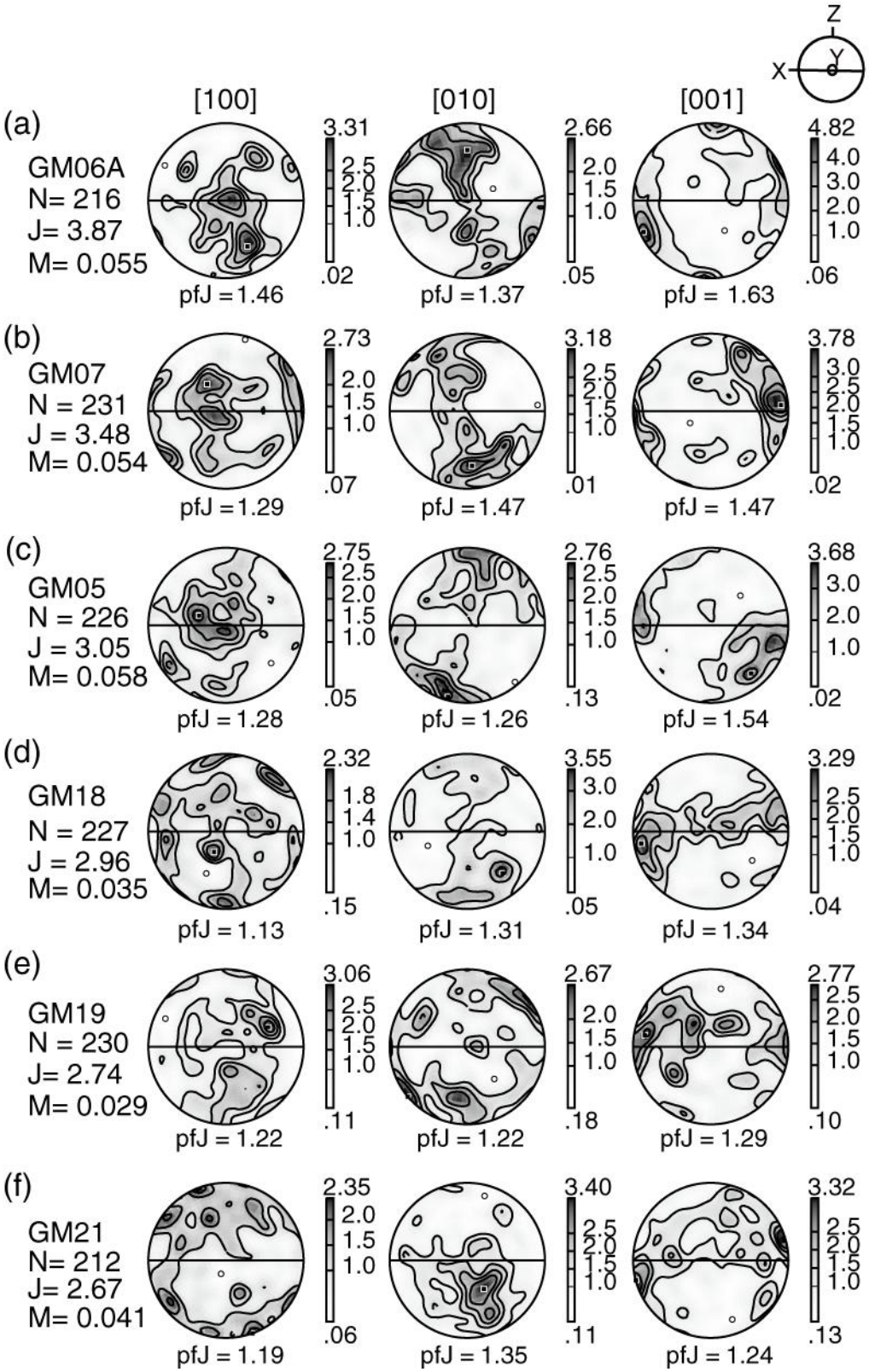

Figure 15. Olivine CPO data of fine-grained texture at Gongen pass.

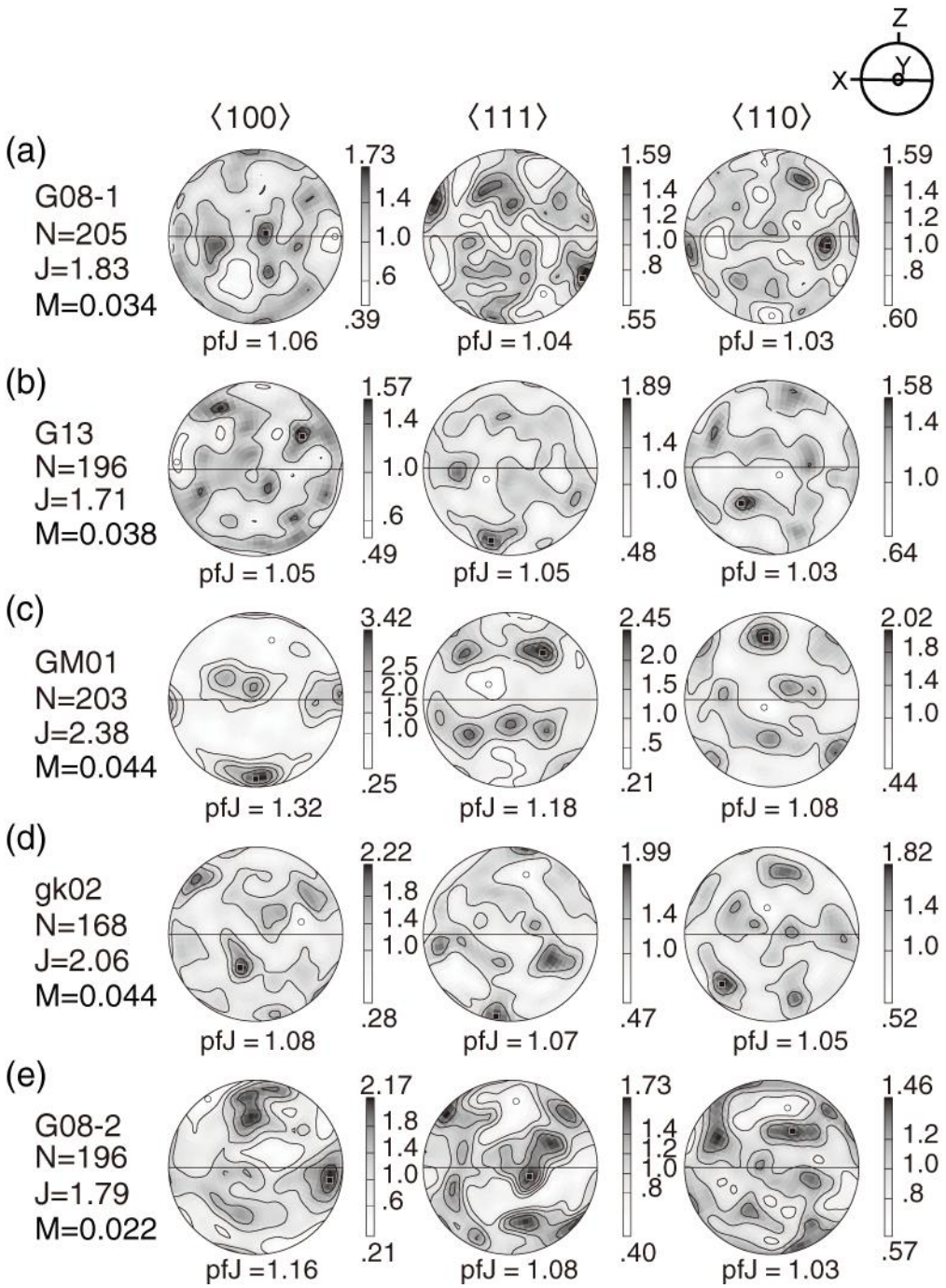

Figure 16. Garnet CPO data. Garnet CPOs are exhibited in descending order of garnet.

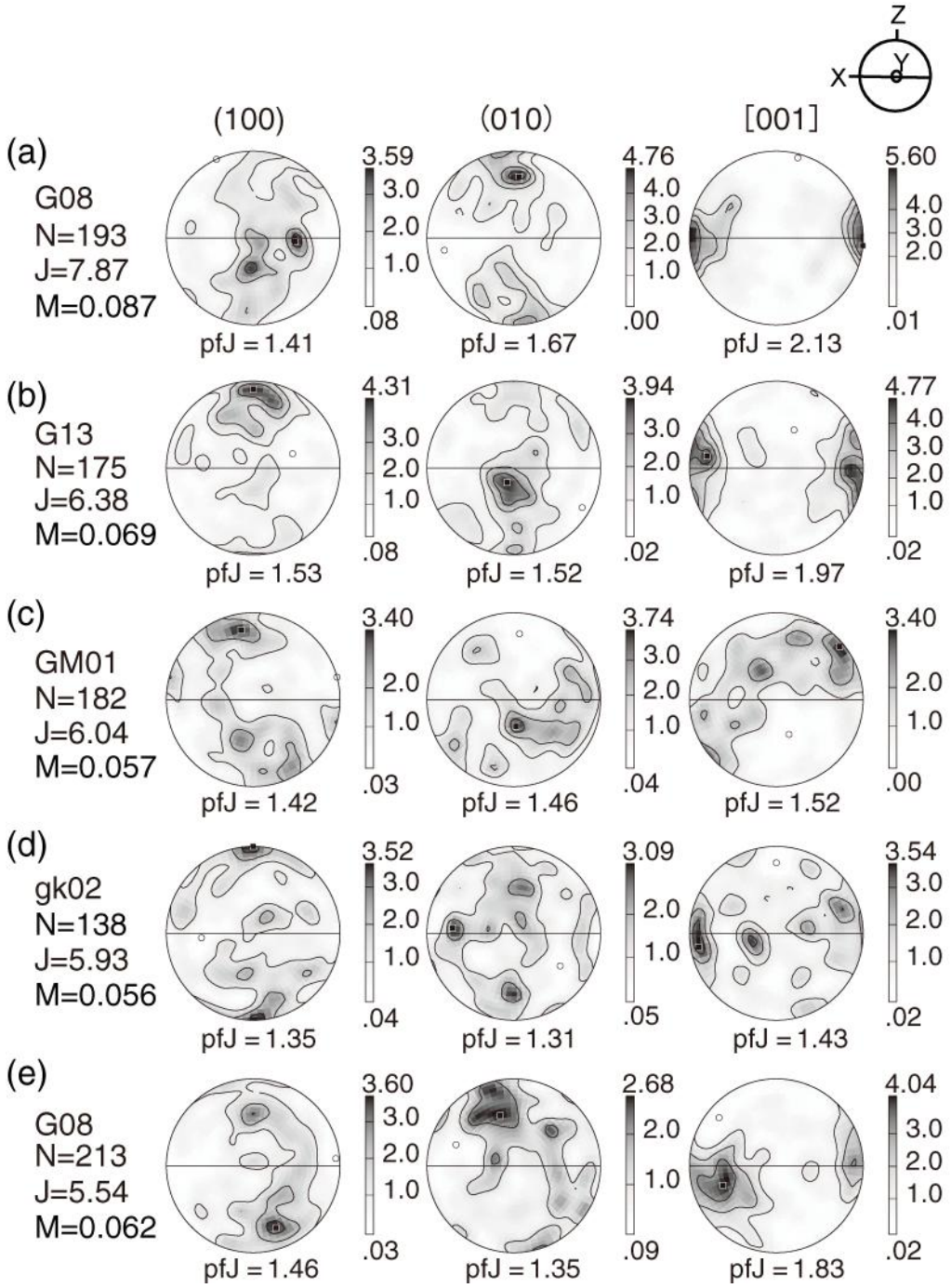

Figure 17. Clinopyroxene CPO data. Clinopyroxene CPOs are exhibited in descending order of garnet.

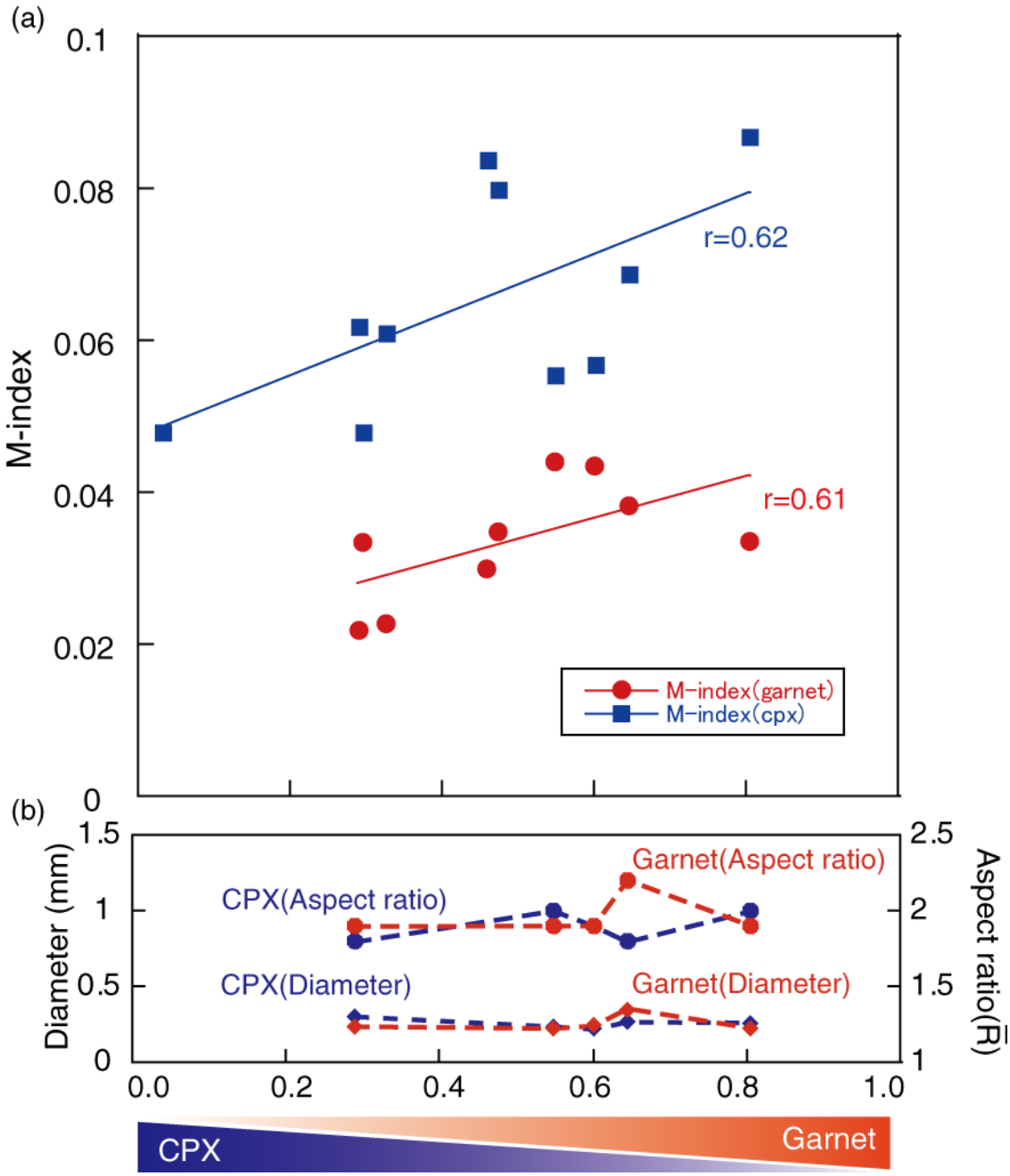

Figure 18. M-index, grain size and aspect ratio of garnet clinopyroxenites with respect to modal composition. (a) M-index vs. modal composition. Red and blue solid line are regression lines of garnet and clinopyroxene, respectively. The 'r' is correlation coefficient. (b) Grain size and aspect ratio vs. modal composition.

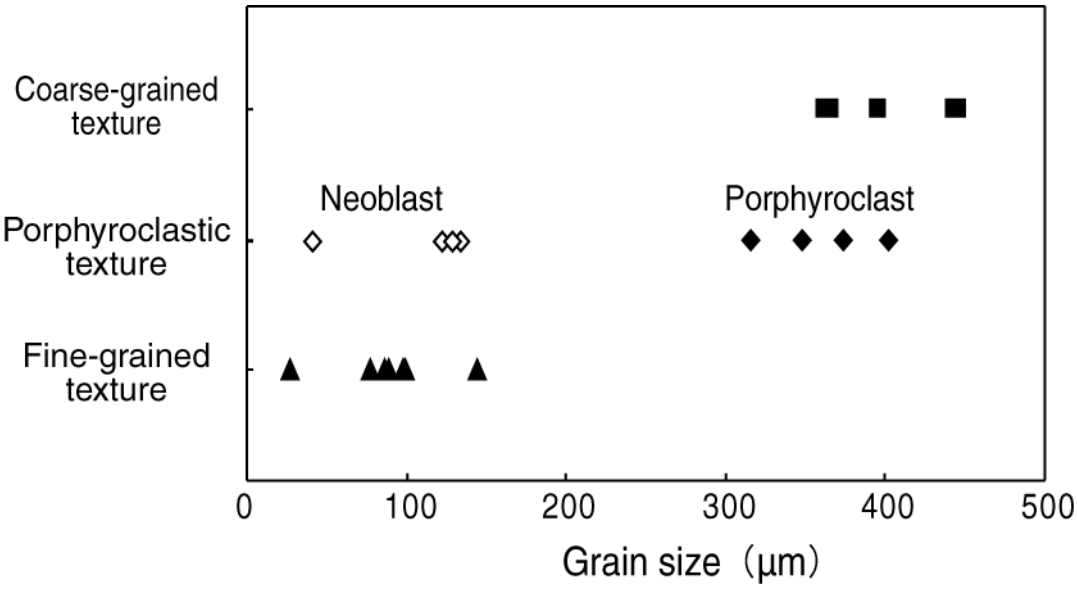

Figure 19. Grain size of olivine for each type of textures. The grain size of porphyroclasts and neoblasts are separately measured.

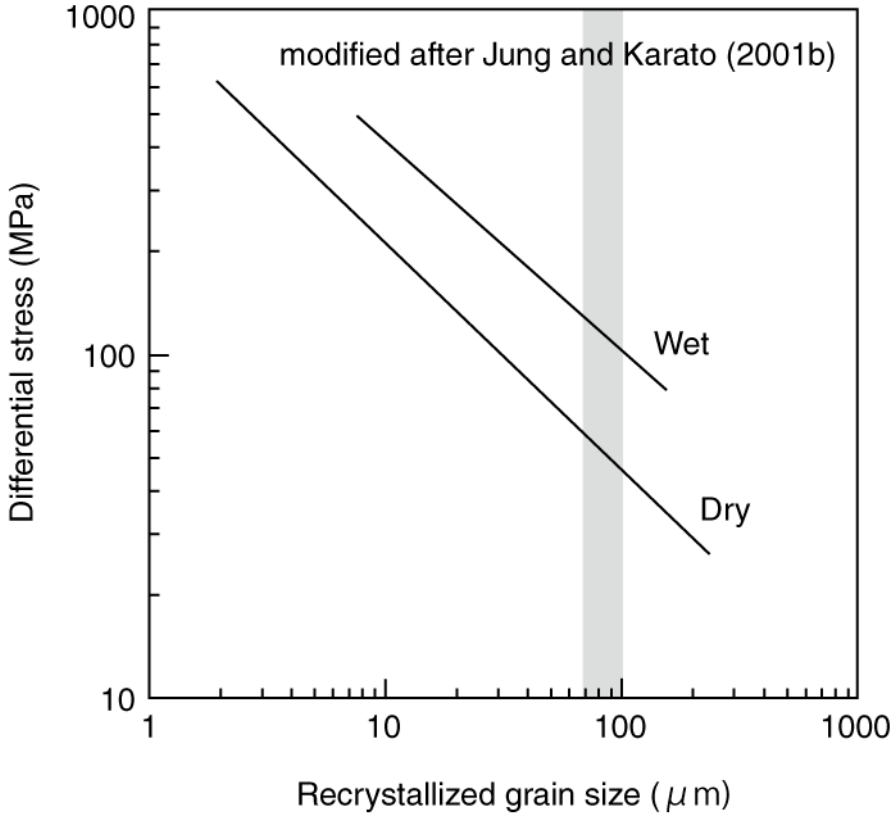

Figure 20. Relationships between differential stress and recrystallized grain size (after Jung and Karato, 2001b). Gray area indicates the mean grain size estimated from the shear zone center.

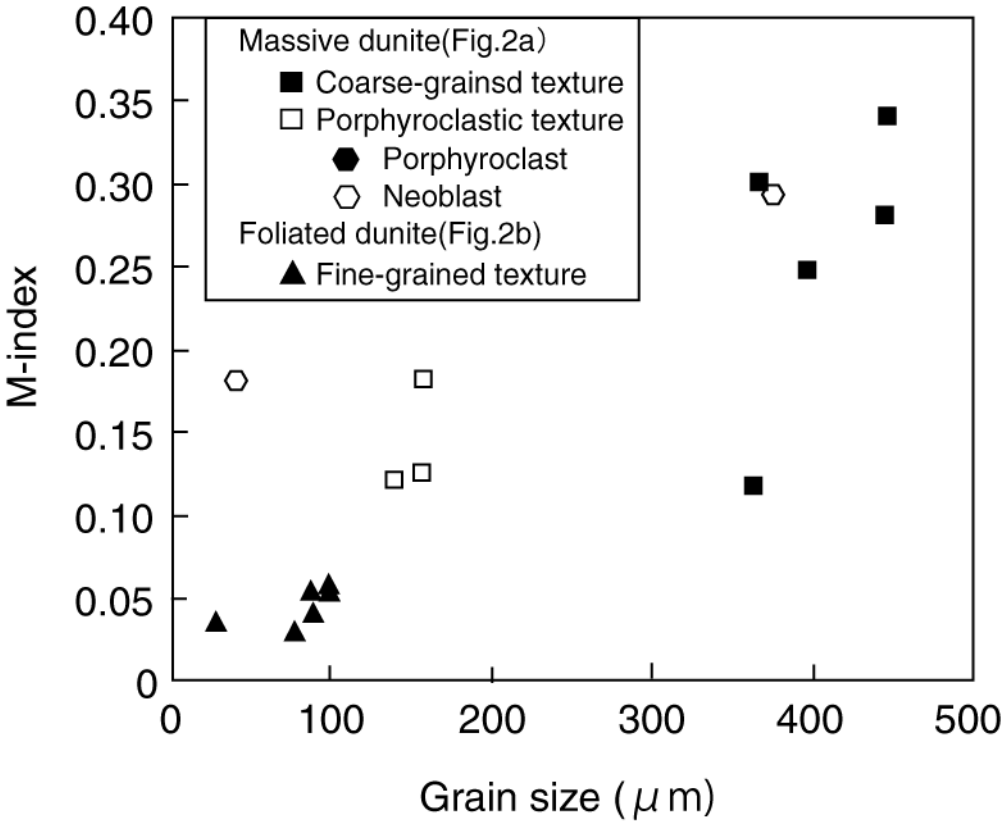

Figure 21. Relationships between grain size of olivine and M-index. In one sample of porphyroclastic texture (HA02), the CPOs of porphyroclasts and neoblasts is separately analyzed.

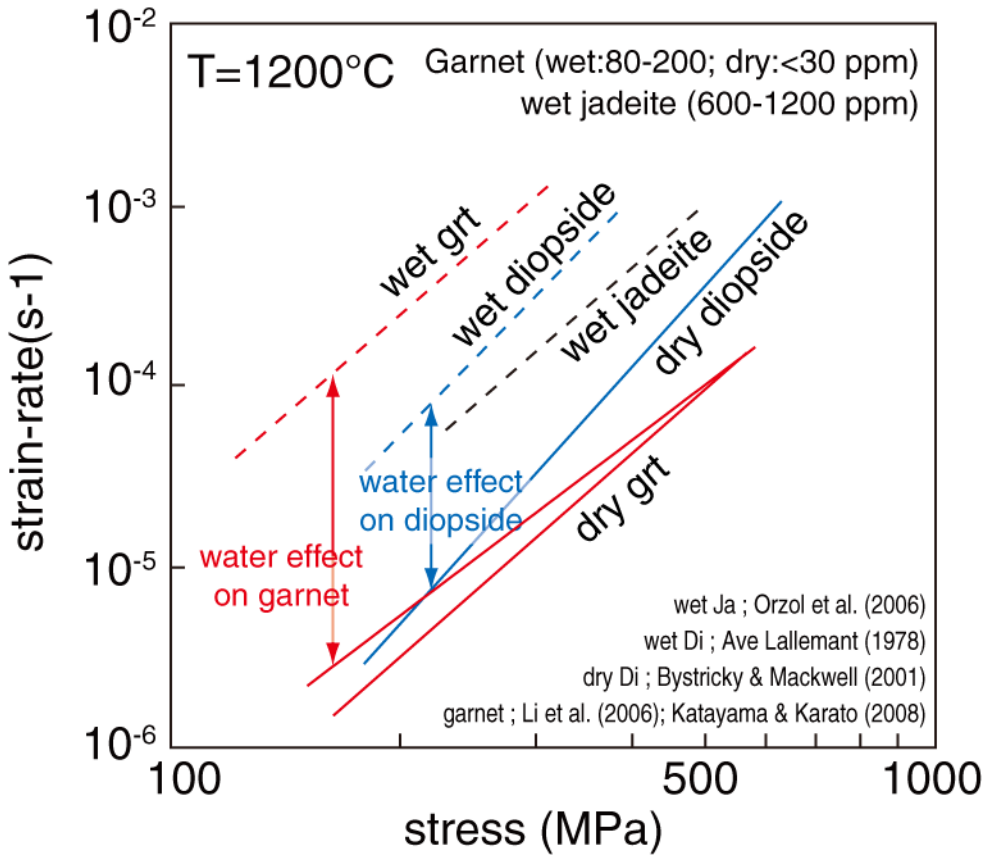

Figure 22. Flow laws of garnet and clinopyroxene. Stress and strain-rate relation of the garnet (Li et al., 2006; Katayama and Karato, 2008) and diopside (dry: Bystricky and Mackwell, 2001; wet: Ave Lallemant, 1978) under dry and wet conditions. Water contents of wet and dry garnet are 80-200 ppm wt. and <30 ppm wt., respectively.

Table 1. Texture and fabric strength of Higashi-akaishi peridotites.

N: Number of grains for olivine CPO. P: porphyroclast. N: neoblast.

Coarse-grained texture	Grain size (μm)	Aspect ratio	N	M-index	J-index
HA03	445.5	2.0	210	0.340	10.2
HA-T0706	366.1	1.8	224	0.300	10
HA-T0704	443.9	1.9	222	0.281	9.59
HA-T0705	395.8	1.9	220	0.248	7.86
HA04	362.5	1.8	232	0.118	5.05
Porphyroclastic texture					
HA02 (P)	373.7	1.8	157	0.293	9.29
HA02-fine (N)	41.3	1.8	222	0.180	5.6
HA01	157.3	1.8	221	0.181	6.2
HA01 (P)	402.2	–	–	–	–
HA01 (N)	134.1	–	–	–	–
HA-T0703	139.3	1.9	247	0.120	4.93
HA-T0703 (P)	348.1	–	–	–	–
HA-T0703 (N)	122.4	–	–	–	–
HA-T0707	156.8	1.8	226	0.125	4.73
HA-T0707 (P)	315.9	–	–	–	–
HA-T0707 (N)	129.1	–	–	–	–
Fine-grained texture					
GM21	88.5	1.8	212	0.041	2.67
GM19	76.8	1.8	230	0.029	2.74
GM18	27.6	1.8	227	0.035	2.96
GM07	86.9	1.6	231	0.054	3.48
GM06A	98.9	1.6	216	0.055	3.87
GM05	98.4	1.6	226	0.058	3.05

Table 2. Texture and fabric strength of Higashi-akaishi garnet clinopyroxenites. N: Number of grains for garnet and clinopyroxene CPOs.

Sample	Phase	Vol %	Grain size (mm)	Aspect ratio	N	M-index	J-index
G06C	garnet	3	–	–	–	–	–
	cpx	97	–	–	221	0.048	4.51
G08-2	garnet	28.9	0.24	1.9	196	0.022	1.79
	cpx	71.1	0.3	1.8	213	0.062	5.54
G08C	garnet	29.4	–	–	208	0.034	1.38
	cpx	70.6	–	–	242	0.048	4.8
G06B	garnet	32.5	–	–	223	0.023	1.59
	cpx	67.5	–	–	209	0.061	5.24
G08D	garnet	45.8	–	–	200	0.030	1.43
	cpx	54.2	–	–	221	0.084	5.43
G08A	garnet	47.2	–	–	229	0.035	1.33
	cpx	52.8	–	–	204	0.080	5.68
gk02	garnet	54.8	0.22	1.9	168	0.044	2.06
	cpx	45.2	0.24	2	138	0.056	5.93
GM01	garnet	60.1	0.25	1.9	203	0.044	2.38
	cpx	39.9	0.22	1.9	182	0.057	6.04
G13	garnet	64.5	0.35	2.2	196	0.038	1.71
	cpx	35.5	0.27	1.8	175	0.069	6.38
G08-1	garnet	80.4	0.22	1.9	205	0.034	1.83
	cpx	19.6	0.26	2	193	0.087	7.87

Table 3. Chemical compositions of minerals.

Thin section no.	G08	G08	G13	GM01	gk02	G08	G08	G13	GM01	gk02
Sample no.	Ga1	Ga2	Ga3	Ga4	Ga5	Cpx1	Cpx2	Cpx3	Cpx4	Cpx5
SiO_2	41.02	40.82	39.64	41.06	40.67	54.43	54.72	53.29	55.30	53.90
TiO_2	0.05	0.04	0.32	0.30	0.09	0.08	0.08	0.33	0.06	0.16
Al_2O_3	22.40	22.70	22.66	23.35	22.10	1.18	1.13	1.33	0.84	2.01
FeO*	14.93	14.91	15.73	14.03	13.92	2.60	2.56	3.19	2.50	2.48
MnO	0.43	0.40	0.81	0.47	0.43	0.02	0.03	0.20	0.05	0.01
MgO	14.05	14.55	13.20	14.99	14.08	16.53	16.63	16.63	17.42	16.24
CaO	6.79	6.26	7.25	5.92	7.64	24.36	24.60	24.56	24.27	24.35
Na_2O	0.00	0.01	0.08	0.06	0.01	0.55	0.51	0.47	0.33	0.58
K_2O	0.00	0.00	0.09	0.09	0.00	0.00	0.00	0.09	0.00	0.01
Cr_2O_3	0.12	0.15	0.15	0.19	0.15	0.09	0.10	0.12	0.00	0.06
NiO	0.01	0.00	0.25	0.22	0.03	0.12	0.03	0.25	0.04	0.04
V_2O_3	0.01	0.05	0.31	0.32	0.06	0.05	0.03	0.32	0.01	0.04
Total	99.81	99.88	100.47	100.99	99.19	100.00	100.41	100.78	100.82	99.88
Cations/O=	12	12	12	12	12	6	6	6	6	6
Si	3.021	3.000	2.937	2.976	3.012	1.982	1.983	1.942	1.991	1.964
Ti	0.003	0.002	0.018	0.016	0.005	0.002	0.002	0.009	0.002	0.004
Al	1.944	1.967	1.978	1.994	1.929	0.051	0.048	0.057	0.036	0.086
Fe	0.919	0.916	0.975	0.851	0.862	0.079	0.078	0.097	0.075	0.076
Mn	0.027	0.025	0.051	0.029	0.027	0.000	0.001	0.006	0.002	0.000
Mg	1.543	1.594	1.458	1.620	1.555	0.897	0.899	0.904	0.935	0.882
Ca	0.536	0.493	0.575	0.460	0.607	0.950	0.955	0.959	0.936	0.950
Na	0.000	0.001	0.012	0.009	0.001	0.039	0.036	0.033	0.023	0.041
K	0.000	0.000	0.008	0.008	0.000	0.000	0.000	0.004	0.000	0.000
Cr	0.007	0.009	0.008	0.011	0.009	0.002	0.003	0.004	0.000	0.002
Ni	0.001	0.000	0.015	0.013	0.002	0.004	0.001	0.007	0.001	0.001
V	0.000	0.003	0.018	0.019	0.004	0.001	0.001	0.009	0.000	0.001
Total	8.000	8.009	8.053	8.004	8.012	4.008	4.007	4.033	4.001	4.008

Table 4. Water contents of garnet.

Sample no.	Thickness (cm)	ν (cm^{-1})	Absorbance	H_2O ppm(wt.)
G08-1	0.0276	3566	0.0344	55
G08-2	0.0276	3567	0.0735	171
G08-3	0.0276	3566	0.0795	184
G08-4	0.0276	3566	0.1254	306
G08-5	0.0276	3573	0.1640	402
G13-1	0.0257	3566	0.0156	17
G13-2	0.0257	3566	0.0141	18
G13-3	0.0257	3566	0.0173	26
G13-4	0.0257	3566	0.0178	36
G13-5	0.0257	3566	0.0193	37
G13-6	0.0257	3566	0.0194	37
G13-7	0.0257	3566	0.0279	56
G13-8	0.0257	3574	0.0377	85
GM01-1	0.0268	3575	0.2821	708
GM01-2	0.0268	3573	0.3558	940
GM01-3	0.0268	3573	0.3786	1000
gk02-1	0.0268	3566	0.0328	48
gk02-2	0.0268	3567	0.0305	49
gk02-3	0.0268	3567	0.0307	52
gk02-4	0.0268	3567	0.0319	54
gk02-5	0.0268	3567	0.0332	55
gk02-6	0.0268	3566	0.0320	57
gk02-7	0.0268	3575	0.0343	63
gk02-8	0.0268	3566	0.0415	72
gk02-9	0.0268	3567	0.0456	87
gk02-10	0.0268	3567	0.0491	93
gk02-11	0.0268	3566	0.0497	103
gk02-12	0.0268	3573	0.0520	110
gk02-13	0.0268	3567	0.0682	144

Table 5. Water contents of clinopyroxene.

Sample no.	Thickness (cm)	ν (cm^{-1})	Absorbance	H_2O ppm(wt.)
G08-P1	0.0276	3454	0.0448	70
		3548	0.0528	
		3649	0.064	
G13-P1	0.0257	3456	0.0709	96
		3541	0.0723	
		3644	0.136	
G13-P2	0.0257	3456	0.0169	60
		3550	0.0307	
		3644	0.0637	
G13-P3	0.0257	3454	0.0515	62
		3539	0.0432	
		3644	0.075	
GM01-P1	0.0268	3456	0.0227	71
		3555	0.0326	
		3644	0.103	
gk02-P1	0.0268	3457	0.0329	43
		3540	0.0369	
		3644	0.083	
gk02-P2	0.0268	3453	0.055	75
		3548	0.066	
		3644	0.0751	
gk02-P3	0.0268	3464	0.0898	92
		3549	0.0795	
		3645	0.118	
gk02-P4	0.0268	3463	0.0557	90
		3548	0.0741	
		3644	0.0703	

Table 6. Flow law data.

	A($MPa^{-n}s^{-1}$)	n	Q(kJ/mol)	Reference
wet gaenet	–	3.4	–	Katayama & Karato (2008)
dry garnet	–	3.4	–	Katayama & Karato (2008)
wet jadeite	$10^{-3.3}$	3.7	326	Orzol et al. (2006)
wet diopside	7.94×10^{-5}	4.3	284	Ave Lallemaunt (1978)
dry diopside	$10^{9.8}$	4.7	760	Bystricky & Mackwell (2001)

The rheological data can be described by a dislocation flow law of the form $\varepsilon = A\sigma^n \exp(-Q/RT)$ where ε is the strain rate, σ is the differential stress, T is the temperature (1200℃), R is the gas constant, and A, n, and Q are empirical parameters for the preexponential term, the stress exponent, and the activation energy for dislocation creep, respectively.